



## THE CDF ARCHIVE: HERSCHEL PACS AND SPIRE SPECTROSCOPIC DATA PIPELINE AND PRODUCTS FOR PROTOSTARS AND YOUNG STELLAR OBJECTS

JOEL D. GREEN<sup>1,2</sup>, YAO-LUN YANG<sup>1</sup>, NEAL J. EVANS II<sup>1</sup>, AGATA KARSKA<sup>3</sup>, GREGORY HERCZEG<sup>4</sup>, EWINE F. VAN DISHOECK<sup>5,6</sup>, JEONG-EUN LEE<sup>7,8</sup>, REBECCA L. LARSON<sup>1</sup>, AND JEROEN BOUWMAN<sup>9</sup>

<sup>1</sup>The University of Texas at Austin, Department of Astronomy, 2515 Speedway, Stop C1400, Austin, TX 78712-1205, USA

<sup>2</sup>Space Telescope Science Institute, Baltimore, MD, USA

<sup>3</sup>Astronomical Observatory Institute, Faculty of Physics, A. Mickiewicz University, Śloneczna 36, 60-286 Poznań, Poland

<sup>4</sup>Kavli Institute for Astronomy and Astrophysics, Peking University, Yi He Yuan Lu 5, Haidian Qu, 100871 Beijing, China

<sup>5</sup>Leiden Observatory, Leiden University, The Netherlands

<sup>6</sup>Max Planck Institute for Extraterrestrial Physics, Garching, Germany

<sup>7</sup>Department of Astronomy & Space Science, Kyung Hee University, Gyeonggi 446-701, Korea

<sup>8</sup>School of Space Research, Kyung Hee University, Yongin-shi, Kyungki-do 449-701, Korea

<sup>9</sup>Max Planck Institute for Astronomy, Heidelberg, Germany

Received 2015 June 26; accepted 2015 December 17; published 2016 February 24

### ABSTRACT

We present the COPS-DIGIT-FOOSH (CDF) *Herschel* spectroscopy data product archive, and related ancillary data products, along with data fidelity assessments, and a user-created archive in collaboration with the *Herschel*-PACS and SPIRE ICC groups. Our products include datacubes, contour maps, automated line fitting results, and best 1D spectra products for all protostellar and disk sources observed with PACS in RangeScan mode for two observing programs: the DIGIT Open Time Key Program (KPOT\_nevans\_1 and SDP\_nevans\_1; PI: N. Evans), and the FOOSH Open Time Program (OT1\_jgreen02\_2; PI: J. Green). In addition, we provide our best SPIRE-FTS spectroscopic products for the COPS Open Time Program (OT2\_jgreen02\_6; PI: J. Green) and FOOSH sources. We include details of data processing, descriptions of output products, and tests of their reliability for user applications. We identify the parts of the data set to be used with caution. The resulting absolute flux calibration has improved in almost all cases. Compared to previous reductions, the resulting rotational temperatures and numbers of CO molecules have changed substantially in some sources. On average, however, the rotational temperatures have not changed substantially (<2%), but the number of warm ( $T_{\text{rot}} \sim 300$  K) CO molecules has increased by about 18%.

*Key words:* infrared: stars – stars: formation – submillimeter: ISM – submillimeter: stars – surveys – techniques: imaging spectroscopy

*Supporting material:* machine-readable table

### 1. INTRODUCTION

It has been long established that protostars and young stars form from the collapse of a dense molecular core, developing through different stages as the relative density, temperature, and composition of the envelope, disk, and protostar shift over time. However, many uncertainties remain in the details of the collapse. Specific conditions during infall and outflow throughout the protostellar stage may drive the conditions in the resulting circumstellar disks and protoplanetary systems, influencing the compositional properties of the planet-forming material. Particularly important is the role played by accretion-driven heating events; whether the accretion process is characterized by gradually diminishing accretion (Offner & McKee 2011) or episodic accretion (e.g., Dunham et al. 2010, 2014; Kim et al. 2012) can have a large impact. In either case, the final disk mass and chemistry may be set by the time spent in relatively high accretion phases; in the case of episodic accretion, the disk mass at the end of the protostellar phase may be determined by the phasing of the last burst of accretion onto the star and the end of infall. Observational constraints on the physical processes in these systems are gained from a multi-wavelength understanding of molecular, atomic, and ionic tracers through optical, infrared, and millimeter-wave telescopes.

Many protostars in relatively nearby ( $d \leq 300$  pc) clouds have been studied extensively in the infrared. The *Infrared*

*Space Observatory*’s Long Wavelength Spectrograph detected gas phase H<sub>2</sub>O, high-*J* CO rotational transitions, and fine structure emission lines toward protostars and related sources (e.g., Ceccarelli et al. 1999; Giannini et al. 1999, 2001; Lorenzetti et al. 1999, 2000; Nisini et al. 2002). These lines trace the innermost regions of the protostellar envelope, exposed to heating by the central object, and the outflow cavity region, where winds and jets may interact with the envelope and the surrounding cloud.

The Spitzer c2d (“Cores to Disks”) and Gould Belt Legacy surveys (Evans et al. 2009, Dunham et al. 2014), along with a survey of the Taurus cloud (Rebull et al. 2010), have produced a rather complete list of young stellar objects within 300 pc. These source lists in turn informed key program surveys in the far-infrared and submillimeter, with the *Herschel Space Observatory*, an ESA space-based telescope with a 3.5-m primary mirror optimized for far-infrared and submillimeter observations. *Herschel*-SPIRE (Spectral and Photometric Imaging REceiver, 194–670  $\mu$ m; Griffin et al. 2010) allowed low resolution spectroscopy over the entire submillimeter domain; the PACS (Photodetector Array Camera and Spectrometer; Poglitsch et al. 2010) instrument provided low-resolution spectroscopy over the far-infrared range. *Herschel* was sensitive to dust continuum, and had access to the full suite of mid-*J* emission lines from CO, HCO<sup>+</sup>, <sup>13</sup>CO, and several low-lying energy states of H<sub>2</sub>O,

which trace the shocked gas in the outflow and the surrounding envelope.

In a previous paper (Green et al. 2013a) we used data from the PACS spectrograph to characterize a sample of well-studied protostars, selected primarily from the c2d sample, including both Class 0 and Class I objects. Class 0 and Class I sources are characterized observationally by rising spectral energy distributions (SEDs) between near-infrared and mid-infrared wavelengths. In addition to the continuum emission, the far-infrared/submillimeter bands contain numerous pure rotational transitions of the CO ladder, as well as low-lying lines of H<sub>2</sub>O, OH, HCO<sup>+</sup>, atomic lines ([C I], [O I]), and ionic lines ([C II], [N II]), all potential tracers of gas content and properties. The transitions and collisional rates of these simple molecules are well-understood (see, e.g., Yang et al. 2010; Neufeld 2012, for a recent update on CO). Thus these lines make excellent diagnostics of opacity, density, temperature, and shock velocities (e.g., Kaufman & Neufeld 1996; Flower & Pineau Des Forets 2010) of the gas surrounding these systems. In a second previous paper (Green et al. 2013b), we combined PACS, SPIRE, and ground-based spectroscopy of stars undergoing episodic accretion events (FU Orionis objects, hereafter FUors) in order to determine their gas and envelope properties post-outburst. Both previous papers used an earlier data reduction pipeline; we will compare results from those papers to those obtained with the new reduction presented here for a few characteristic quantities in Section 5.3.

This paper describes the CDF (COPS-DIGIT-FOOSH) archive, with *Herschel*-PACS and SPIRE spectroscopic observations of 70 objects (protostars, young stellar objects, and FUors) from the “Dust, Ice, and Gas in Time” (DIGIT Key Project), “FU Orionis Objects Surveyed with *Herschel*” (FOOSH OT1), and “CO in Protostars” (COPS OT2) *Herschel* programs. These have been delivered to the *Herschel* archive and are available. Here we describe the reduction methods and the data products. The full source list is shown in Table 1.

We use data products from the HIPE 13/CalTree 65 pipeline, provided by the *Herschel* Science Center, the most current version at the time of reprocessing during summer 2014. The most notable new feature in this reduction of PACS spectroscopy is a correction for pointing and jitter offsets during observations. The SPIRE spectra are also enhanced by the use of a correction for semi-extended sources (Wu et al. 2013). The spectra are reduced and analyzed using automated routines optimized for *Herschel* to detect line emission and continuum properties. We provide spectroscopic data cubes, line fluxes, continuum analysis, and error analysis across all spatial positions observed in these 70 sources. In addition to this paper, a full description of the pipeline and details of this archive can be found in the web release of the data to the *Herschel* Science Archive (HSA) User Provided Data Products<sup>10</sup>, upcoming analysis papers (J. Green et al. 2016, in preparation), and a paper on 3D radiative transfer modeling of a single source (the protostar BHR71; Y.-L. Yang et al. 2016, in preparation). The corresponding *Spitzer* data can mostly be found in IRS\_Disks and c2d spectroscopic programs (Lahuis et al. 2006). Finally we note that this analysis could be expanded to include all objects observed in similar modes, and the automated routines adapted to other (non-*Herschel*) data sets.

<sup>10</sup> <http://www.cosmos.esa.int/web/herschel/user-provided-data-products>

## 2. OBSERVATIONS

### 2.1. Dust, Ice, and Gas In Time (DIGIT)

The full DIGIT spectroscopic sample consists of 63 sources: 24 Herbig Ae/Be stars (intermediate mass sources with circumstellar disks), 9 T Tauri stars (low mass young stars with circumstellar disks), and 30 protostars (young stars with significant envelope emission) observed with PACS spectroscopy. The distribution in luminosity and characteristic temperature are shown in Figure 1. DIGIT also included an additional wTTS (weak-line T Tauri star) sample that was observed photometrically and delivered separately. The wTTS sample is fully described by Cieza et al. (2013).

The full DIGIT embedded protostellar sample consisted of 30 Class 0/I targets, drawn from previous studies, focusing on protostars with high-quality *Spitzer*-IRS 5–40  $\mu\text{m}$  spectroscopy (summarized by Lahuis et al. 2006), and UV, optical, infrared, and submillimeter complementary data. Two sources (IRS44 and IRS46) were observed in a single pointing centered on IRS46. These objects are selected from some of the nearest and best-studied molecular clouds: Taurus (140 pc; 6 targets), Ophiuchus (125 pc; 7 targets), Perseus (230–250 pc; 7 targets), R Corona Australis (130 pc; 3 targets), Serpens (429 pc; 2 targets), Chamaeleon (178 pc, 1 target), and 4 additional isolated cores. The sources span two orders of magnitude in bolometric luminosity, from  $L_{\text{bol}} = 0.11$  to 27.8  $L_{\odot}$ . The photometric fluxes of embedded protostellar sample at 100  $\mu\text{m}$  span two orders of magnitude as well, from 1.0 to 240.1 Jy. In terms of the usual tracers of evolutionary development, the bolometric temperatures range from  $T_{\text{bol}} = 27$  to 592 K, spanning the Class 0/I divide at  $T_{\text{bol}} = 70$  K. The ratio of  $L_{\text{bol}}$  to the luminosity at  $\lambda \geq 350 \mu\text{m}$  ranges from  $L_{\text{bol}}/L_{\text{smm}} = 5$  to  $>10,000$ , with most ratios (18 of 22 with well-constrained submillimeter data) falling between 10 and 1000. The disk sources were selected as bright targets for PACS spectral scans.

PACS is a  $5 \times 5$  array of  $9.^{\prime\prime}4 \times 9.^{\prime\prime}4$  spatial pixels (hereinafter referred to as “spaxels”) covering the spectral range from 50 to 210  $\mu\text{m}$  with  $\lambda/\Delta\lambda \sim 1000$ –3000, divided into four segments, covering  $\lambda \sim 50$ –75, 70–105, 100–145, and 140–210  $\mu\text{m}$ . The PACS spatial resolution ranges from  $\sim 9''$  at the shortest wavelengths (50  $\mu\text{m}$ ) to  $\sim 18''$  at the longest (210  $\mu\text{m}$ ), corresponding to 1000–4500 AU at the distances of most sources. The nominal pointing rms of the telescope is  $2''$ .

For the DIGIT embedded protostars sample we utilized the full range of PACS (50–210  $\mu\text{m}$ ) in two linked, pointed, chop/nod rangescans: a blue scan covering 50–75 and 100–150  $\mu\text{m}$  (SED B2A + short R1); and a red scan covering 70–105 and 140–210  $\mu\text{m}$  (SED B2B + long R1). We used 6 and 4 range repetitions respectively, for integration times of 6853 and 9088 s (a total of  $\sim 16,000$  s per target for the entire 50–210  $\mu\text{m}$  scan). Excluding overhead, 50% of the integration time is spent on source and 50% on sky. Thus the effective on-source integration times are 3088 and 4180 s, for the blue and red scans, respectively. The total on-source integration time to achieve the entire 50–210  $\mu\text{m}$  scan is then 7268 s.

The telescope and sky background emission was subtracted using two nod positions  $6'$  from the source in opposite directions. The telescope chopped between the source and nod positions, cycling every 1/8 of a second in a pre-determined pattern of on and off positions (Poglitsch et al. 2010) during the integration.

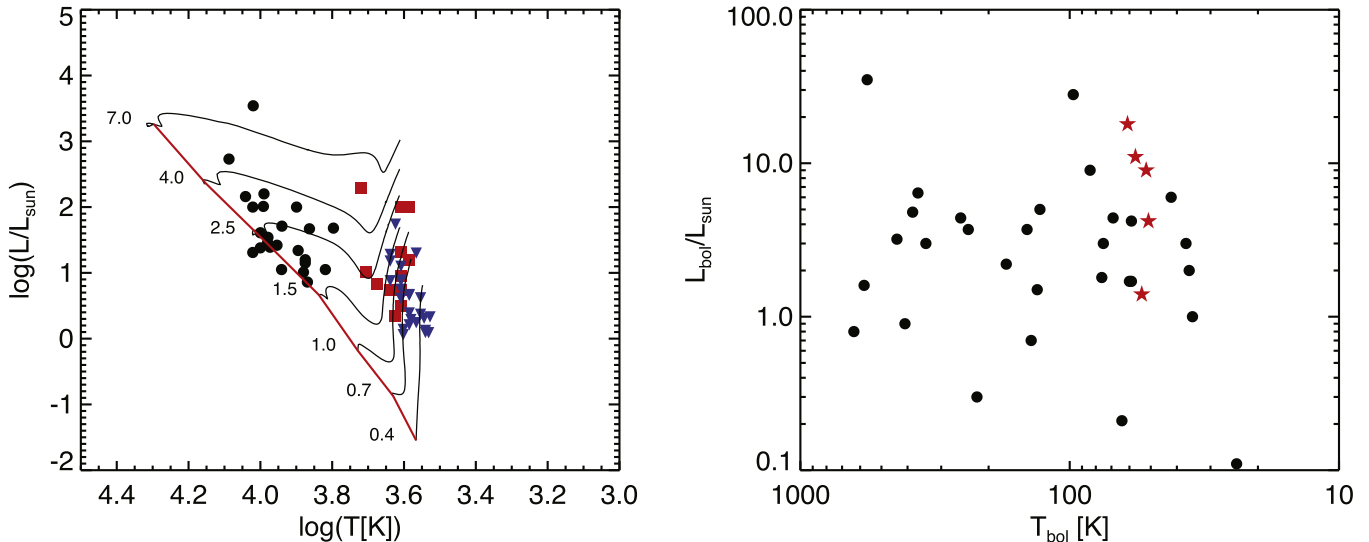


**Figure 1.** Left: range of stellar temperature and  $L_{\text{bol}}$  for the disk sample, superimposed on the HR diagram with evolutionary tracks by Palla & Stahler (1993). The filled black circles indicate our Herbig Ae sample, the red squares indicate the HR diagram positions of our classical T Tauri star (cTTS) sample, and the blue triangles denote the positions of our wTTS sample. Right: range of  $T_{\text{bol}}$  and  $L_{\text{bol}}$  for the embedded sample. Red stars indicate sources observed by the “WISH” key program with PACS full spectral scans.

Most (21 of 33) disk sources were observed with the same procedure as the embedded objects. The other 12 sources have only partial spectral coverage: 8 Herbig Ae/Be sources (HD 35187, HD 203024, HD 245906, HD 142666, HD 144432, HD 141569, HD98922, and HD 150193) and 4 T Tauri sources (HT Lup, RU Lup, RY Lup, and RNO90) were observed using only the blue scans (i.e., achieving a wavelength coverage only from SED B2A + short R1, 100–150  $\mu\text{m}$ ). 9 of these 12 sources (all except HD 35187, HD 203024, and HD 245906) were observed in a further limited wavelength range (60–72 + 120–134  $\mu\text{m}$ ; referred to as “forsterite only” scans for their focus on the 69  $\mu\text{m}$  forsterite dust feature). This procedure allowed shorter integration times to achieve the same signal-to-noise ratio (S/N) in the covered regions.

## 2.2. FU Orionis Objects Surveyed with *Herschel* (FOOSH)

FUors are low-mass pre-main sequence objects named after the archetype FU Orionis (hereafter, FU Ori), which produced a 6 magnitude outburst at  $B$ -band in 1936 and has remained close to peak brightness ever since. The FOOSH program consisted of 21 hrs of *Herschel* observing time: V1057 Cyg, V1331 Cyg, V1515 Cyg, V1735 Cyg, and FU Ori were observed as part of FOOSH and analyzed from preliminary data reduction (Green et al. 2013b).

For the FOOSH sample we again utilized the full range of PACS (50–210  $\mu\text{m}$ ) in two linked, pointed, chop/nod rangescans: a blue scan covering 50–75 and 100–150  $\mu\text{m}$  (SED B2A + short R1); and a red scan covering 70–105 and 140–210  $\mu\text{m}$  (SED B2B + long R1). We used 6 and 4 range repetitions respectively, for integration times of 3530 and 4620 s (a total of  $\sim$ 8000 s per target and off-positions combined, for the entire 50–210  $\mu\text{m}$  scan; the on-source integration time is  $\sim$ 3000 s). The telescope sky background was subtracted using two nod positions 6' from the source.

The SPIRE-Fourier Transform Spectrometer (FTS) data were taken in a single pointing with sparse image sampling, high spectral resolution mode, over 1 hr of integration time. The spectrum is divided into two orders covering the spectral

ranges 194–325  $\mu\text{m}$  (“SSW”; Spectrograph Short Wavelengths) and 320–690  $\mu\text{m}$  (“SLW”; Spectrograph Long Wavelengths), with a resolution,  $\Delta\nu$  of 1.44 GHz and resolving power,  $\lambda/\Delta\lambda \sim 300$ –800, increasing at shorter wavelengths (Griffin et al. 2010). The FOOSH data were observed in a single pointing with sparse image sampling, high spectral resolution, in 1 hr of integration time per source.

## 2.3. CO in ProtoStars (COPS)

The sample of 31 “COPS” protostars observed with SPIRE-FTS includes 25 sources from the DIGIT and 6 from the WISH (Water in Star-forming regions with *Herschel*, PI: E. van Dishoeck; van Dishoeck et al. 2011; see also Nisini et al. 2010; Kristensen et al. 2012; Karska et al. 2013; Wampfler et al. 2013) key programs. A nearly identical sample was observed in CO  $J = 16 \rightarrow 15$  with HIFI (PI: L. Kristensen) and is presented in L. Kristensen et al. 2016, (in preparation). This data set (COPS: SPIRE-FTS) is analyzed in a forthcoming paper (J. Green et al. 2016, in preparation). The SPIRE beamsize ranges from 17'' to 40'', equivalent to physical sizes of  $\sim$ 2000–10,000 AU at the distances of the COPS sources, comparable to the size of a typical core (Ward-Thompson et al. 2007, p. 33) but smaller than many collimated outflows.

The COPS SPIRE-FTS data were observed identically to the FOOSH SPIRE data, in a single pointing with sparse image sampling, high spectral resolution, in 1 hr of integration time per source, with one exception: the IRS 44/46 data were observed in medium image sampling (e.g., complete spatial coverage within the inner 2 rings of spaxels), in 1.5 hr, in order to better distinguish IRS 44 (the comparatively brighter IR source; Green et al. 2013a, J. Green et al. 2016, in preparation) from IRS 46.

## 2.4. Overview of the Products

The basic data products we produce for each source observed with PACS and SPIRE spectroscopy are the following:

1. Datacubes (wavelength versus flux density versus spatial position), with advanced corrections from HIPE 13.
2. Best-calibration 1D spectra for point sources and marginally extended sources within the data cube, including flat spectra (continuum-subtracted), continuum (line-subtracted), and residual spectra.
3. Line identification and fitted parameters obtained with an automated fitting routine (for both 2D and 1D spectra), organized by spatial position for each source, including a complete, sortable linelist.
4. Contour plots for extended line and continuum emission.
5. EPS files for the last three products above, allowing users to verify all automated fits.

In this document, we review the archive data processing and products in detail. First we describe the custom data reduction pipeline we used in Section 3. Second, we describe the automatic line fitting routine and the line fitting results in detail in Section 4. Third, we describe the data products and output file format, including post-processing data products in Section 5. Lastly, we summarize the results of this archive in Section 6. Our line source libraries and a full inventory of sources included in this archive are shown at the end of this paper, in the [Appendix](#).

### 3. PIPELINE SETTINGS

#### 3.1. PACS Pipeline for Pointlike and Small Sources

We begin with the `hipe13.0.1006.ChopNodPointingCorrection.py` pipeline script (the “Point Source Background Normalization” script). This script was made available in HIPE 13; any version of HIPE 13 should work for this purpose. We then made the following modifications:

1. The script is run as a loop over numerous OBSIDs for blue and red cameras.
2. We make an adjustment in the pipeline to account for the effects of pointing jitter (changes in pointing offset during the course of the observation). The chi-squared difference between the flux of the “point” source and the flux of the centered beam, via a map/grid, is determined using the beams of calibration products. We define the “oversample” (the samples per spatial element in each dimension, improving precision of positional determination) and the “smoothFactor” (smoothing in the spectral domain, in terms of grating positions rather than wavelength). For the pipeline, we set these to `oversample = 8` and `smoothFactor = 7`; using larger values yielded no apparent benefit.
3. In the `specFlatFieldRange` command, we decrease “polyOrder” to 4 (from the default of 5). This slightly improves memory usage, although the effect is minor. There is no impact on the success of the flatfielding.
4. We select `excludeLeaks = True` so that we do not use the light-leakage affected regions for flatfielding. These regions are not reported in the final spectral product, which removes the 95–105  $\mu\text{m}$  range (and a few spectral lines including CO  $J = 25 \rightarrow 24$  in that region). The advantage to removing these data is that we avoid the typically erratic continuum in that region when determining the flatfielding correction.
5. We change the “gaussianFilterWidth” to 35 (instead of 50). This parameter is the number of wavelength points

over which we assess the scaling of the central spaxel to the level of the  $3 \times 3$  spaxel set, which is used in the production of the “ $3 \times 3$ YES” product, below; it is an attempt to correct for the shape of the continuum, picking a width large enough to account for pointing jitter but not so wide as to smooth out the actual continuum shape. By using the flux of the “ $3 \times 3$ ” central 9 spaxels, and comparing to a true point source distribution, we correct for the movement of the flux centroid throughout the observation, referred to as pointing jitter. The number is essentially based on the sampling and the significance of pointing jitter, for a particular observation; we settled on a value of 35 through trial-and-error testing.

6. We add a “garbage collection” line at the end of the loop. This allows us to run at least 200 OBSIDs within a single command, given sufficient disk space. It takes about 1 hour/OBSID to run at these settings on a (early 2014) 12-core processor with 96 GB of RAM dedicated to the process, excluding data download time; for a total of 200 OBSIDs, we required 200 CPU hours (e.g., 2 weeks) to reduce all the targets in our sample.

The default pipeline reduction shows significant mismatches between red and blue modules, and it frequently did not align with photometry or with SPIRE observations of the same position. The early pipelines did not fully account for source spatial extent or pointing jitter, and the relative spectral response function did not work well at the edges of each order (see e.g., Green et al. 2013a). All of these effects are accounted for in the new pipeline, which has dramatically improved the continuum calibration for PACS in particular. Our new pipeline includes updated calibration data, improved flatfielding, and jitter correction, and other small improvements.

An example of the improvement in spectral/continuum shape, and inter-module flux calibration from the newer pipeline and the jitter correction is shown (for IRAS 12496) in Figure 2. The observations of this source were mis-pointed by about 0.5 spaxel, so it provides a good test. The jitter correction (blue) has removed several spurious broad features and improved overall flux calibration when compared with the non-corrected spectrum (red) or the default pipeline spectrum (black). The absolute flux calibration has also improved considerably. As an example, we consider the improvement to the continuum shape and absolute flux calibration shown for the protostar L1157, a source we will use for most of the following comparisons. Figure 3 demonstrates the improvement. Our best products from the new pipeline results match much better with photometry extracted from archival *Herschel*-PACS and SPIRE imaging of our sample objects in the HSA, from a variety of programs, including: `KPGT_pandre_1`, `KPGT_okrause_1`, `OT1_jtobin_1`, `OT1_jgreen02_1`, and `OT1_mdunham_1`. These data were less subject to saturation problems than data from earlier missions or large beam sizes (e.g., *Spitzer*-MIPS, IRAS). The photometry data are extracted with the source size fitted by the spectroscopic (HIPE) pipeline, at the appropriate waveband (70, 100, 160, 250, 350, or 500  $\mu\text{m}$ ). The data products from which we extracted our photometry have absolute flux calibration uncertainties of <7% for PACS against stellar models (Balog et al. 2014) and asteroid standards (Müller et al. 2014) and 4% for SPIRE when compared against models of Neptune (Bendo et al. 2013), with a 5% uncertainty in cross-calibration between PACS and SPIRE (Müller et al. 2014).

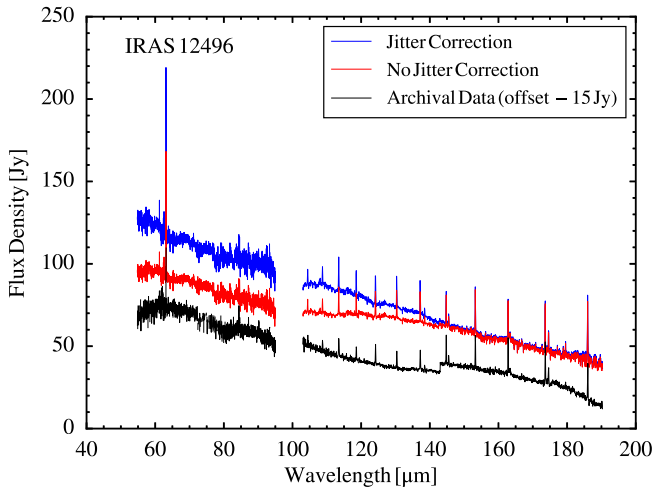


**Figure 2.** The comparison of spectra of IRAS 12496 with different corrections applied. The archival data from HSA processed with the default pipeline are shown in black, offset by  $-15\text{ Jy}$  to separate it from the others. The offsets between modules and the incorrect shape at long wavelengths make searches for broad solid-state features impossible. Our reduction without jitter correction is shown in red; it improves the long wavelength behavior and module matching, but the no-jitter corrected spectrum shows a flattening around  $130\text{ }\mu\text{m}$  that could be mistaken for a solid-state feature. The blue curve shows the result after jitter correction; the broad feature around  $130\text{ }\mu\text{m}$  has been eliminated.

Although L1157 is a typical example, we compared the absolute flux calibration of our final PACS products with the default pipeline products in Figure 4 (top), relative to photometric observations, for all non-confused, protostellar sources of which the photometry was available in the HSA—about one third of our sources. The spectra in this archive are convolved with corresponding photometry filters before comparing with photometric data. The data from HSA were processed with HIPE 11 by *Herschel* Science Center and collected at mid-2014. The flux is scaled from the spectra of central spaxel to the total flux within the central  $3 \times 3$  spaxel to match with the flux of our corrected 1D spectra. The black line indicates a perfect agreement between photometry and spectroscopy; the blue points are values derived from our new products, and the red points are derived from default 2014 HSA products; the enhanced products show much smaller deviation from the photometric values. The products from our archive have a better agreement between the photometry and spectrophotometry. A straight line fitting with data (blue) from our archive shows only a small deviation toward faint sources and without a significant offset to the equality line. Compared to the default HSA products, the dispersion in the residual of line fitting of the CDF products is greatly reduced, from 0.42 to 0.1. The improved reduction has produced reliable spectrophotometry for most sources that are not in confused regions.

Overall, the jitter correction was successfully performed for  $\sim 80\%$  of our sources. The advanced pipeline with jitter correction matches the fluxes by matching the minor mispointings at different wavelengths. However, not every spectrum was improved by the correction. Among the embedded sources in our sample, we got very poor results from the jitter correction on 14 sources: IRAM 04191, L1014, L1455-IRS3, RCRA-IRS5A, RCRA-IRS7C, IRS 46, Serpens-SMM4, EC 82, HD 98922, HD 245906, HD 203024, HT Lup, HD 142666, and HD 35187. The common threads between

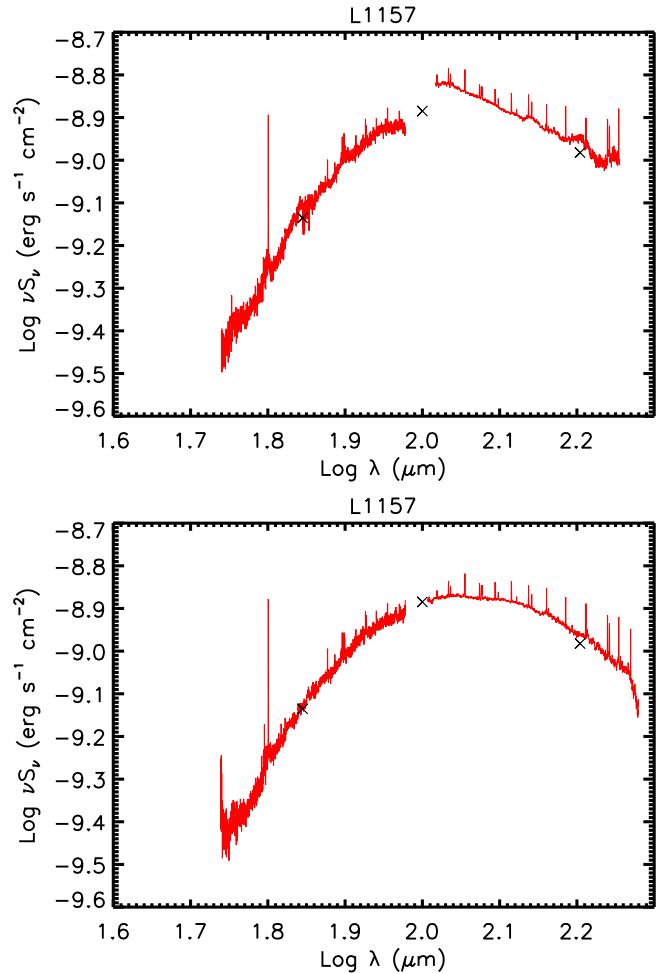


**Figure 3.** Improvement in data quality using new techniques, illustrated for L1157. The top plot shows the old (i.e., the 2012-13 era pipeline and calibration, without jitter correction and flatfielding correction) reduction without scaling. Photometric data (labeled by  $\times$  symbols) obtained later shows a substantial discrepancy. The bottom plot shows the results of the new reduction which produces smoother spectra and better agreement with photometry, without applied scaling. The flatfield corrections have also removed most of the false “solid-state features.” Note that published spectra from 2012-13 typically have scaling applied in post-processing.

these sources are twofold: all have either A) complicated PACS fields in which the central source is not the brightest object, or B) weak continuum ( $< 3\text{ Jy}$  at  $60\text{ }\mu\text{m}$ ). For these sources, we include only the “non-jitter corrected” versions in our archive. This method assumes that the lines and continuum are distributed similarly. Lines with very different distribution require special attention (e.g., Je et al. 2015).

In two embedded sources, we found significant (10%) flux mismatches between the two OBSIDs merged to form the spectrum: L1551-IRS5 (in which the observations were separated by 1.5 years); and GSS30-IRS1 (which shows complicated behavior at long wavelengths; Je et al. 2015). In addition, slight mismatches are noted in L1448-MM (a partially blended chain of sources; Lee et al. 2013).

We find excellent flux matches between modules in all other sources, including all disk/point sources, even in cases with up to 0.5 spaxel mispointings (e.g., TMC1A, IRAS 12496, TMR1, and L1527). Note that we apply no “by-hand” manual scaling after the pipeline reduction.

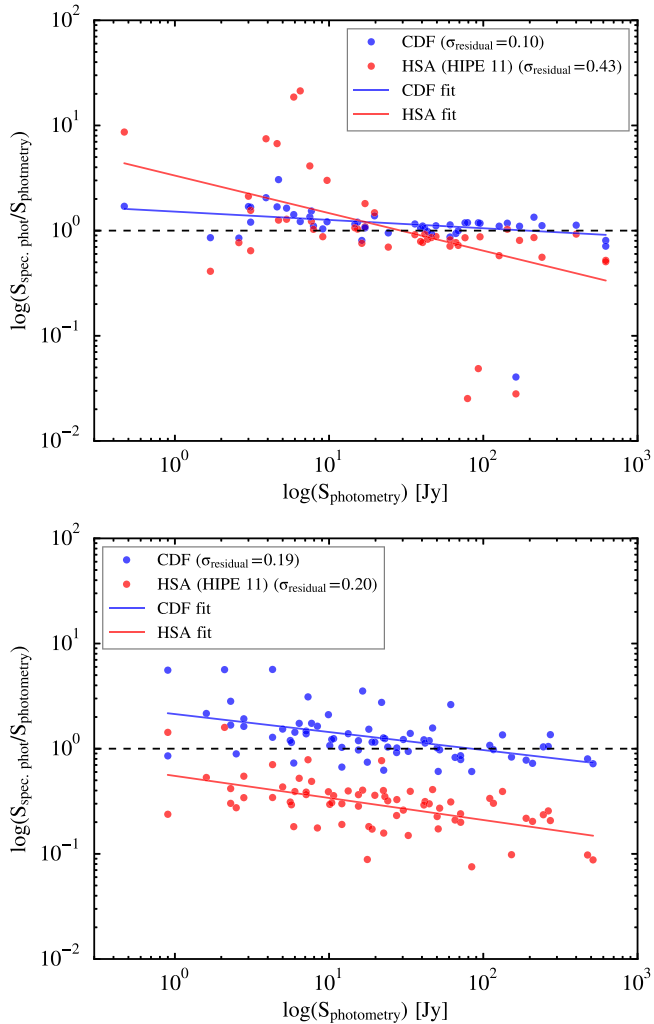


**Figure 4.** Comparison of spectral flux density with photometric flux density, for both the COPS-DIGIT-FOOSH archive and *Herschel* Science Archive (HSA) products. For PACS, shown in the top figure, data are collected from  $\sim 1/3$  of total sources in our archive—all non-confused protostars for which we have gathered photometry data. For SPIRE, shown in the bottom figure, data are collected from 21 sources among 31 COPS sources for which we have gathered photometry data. Data from our archive are shown in blue, while data from the HSA are shown in red. The data from the HSA were processed in the HIPE 11 pipeline and collected in mid-2014. The  $\sigma$  parameter presented in the box is a measure of the deviation from the line of equality, normalized to the mean flux density. Spectra in our archive agree better with the photometric data, while the spectra from the HSA show larger deviations. The blue line is a fit to the data from the CDF archive only; the red line is a fit to the HSA data only. The significant outlier at the bottom right corner is excluded in this fitting. For both PACS and SPIRE, the CDF results are consistent with the equality line, while the HSA archive products are not.

### 3.2. SPIRE Pipeline for Pointlike and Semi-extended Sources

SPIRE used an FTS spectrometer with an onboard calibration source; separate modules were used for short (SSW) and long (SLW) wavelengths. Each module was reduced separately within HIPE version 13.0 using the standard pipeline for extended sources, including apodization. Originally, SPIRE had a spectral resolution of 1.2 GHz. Because the signals are recorded in the Fourier domain, the line would appear as a sinc function with a spectral resolution of 1.2 GHz. After apodization, the spectral response becomes Gaussian-like, but the spectral resolution is degraded to 1.44 GHz.

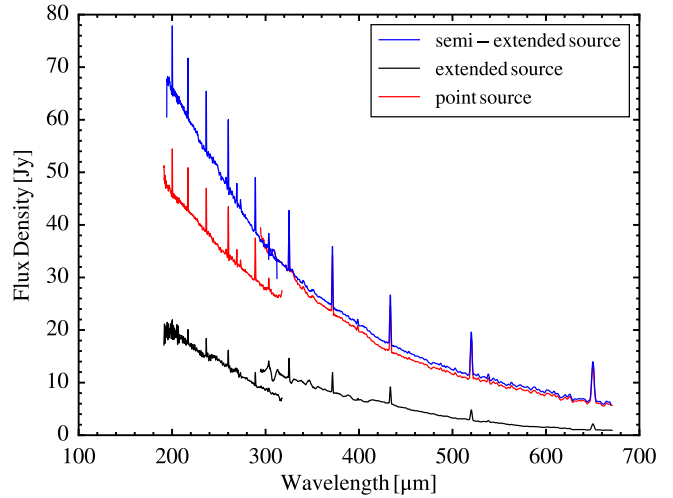


**Figure 5.** Comparison of L1157 SPIRE spectroscopy calibrated with different correction methods: extraction as a point source (red), an extended source (black), and after the semi-extended source correction (blue).

Unlike the case of the PACS pipeline, no significant modifications were made to the basic pipeline script, except for allowing it to run in a loop and for the separate post-processing step to improve the calibration for semi-extended sources. The SPIRE data were extracted using the “extended source” calibration pipeline, as this produced a smoother continuum between modules, better S/N, and fewer spectral artifacts than the “point source” pipeline (Figure 5). We performed post-processing within HIPE version 13.0.1006, using SPIRE calibration data set 12. Starting from the baseline data products, we used the “SemiExtendedSourceCorrector” script, which minimizes the mismatch between SLW and SSW. This semi-extended source correction calibrates sources that are partially resolved by the SPIRE beam. The correction fits a source size based on the assumed source profile to minimize the ratio of SLW and SSW at the overlapped wavelength and then calculates the spectrum within a 40'' Gaussian reference beam, which is independent of wavelength (Wu et al. 2013). This procedure greatly improves the match of the two modules within SPIRE (as it was designed to) and also smooths the continuum (compare Figures 5 and 15 (bottom) for L1157). We applied the “semi-extended source” calibration to all but a few sources (HH 100, IRS 46, and V1735 Cyg) that were excluded owing to their poor spectral quality.

The SPIRE spectrophotometric and photometric fluxes, when extracted in the same reference beam, match to within 5% in 21 of 32 protostars and 2 of 3 FUors. The other 12 sources show varying degrees of mismatch with the photometry. The spectra of B1-a, GSS 30-IRS1, IRAS 03301, and L723-MM overestimate the photometry by 10%–20%; the reverse is true for L483 and IRAS 15398; these are within formal uncertainties for the spectral flux calibration, and are likely attributable to complicating extended emission. V1331 Cyg shows a larger mismatch at 250  $\mu$ m, exceeding the photometric point by 50%; the arclike extended structure associated with this compact source may be the cause. The 250  $\mu$ m photometry for WL 12 and L1455-IRS3 seems suspect. Finally, the IRS 44/46 combined field cannot be fully disentangled; the “IRS 46” SED is contaminated by IRS 44 for  $\lambda > 70 \mu\text{m}$ ; the “IRS 44” SED is missing substantial flux at all

wavelengths due to the position of IRS 44 near the edge of the PACS field of view.

Figure 4 (bottom) shows the comparison of 21 sources for which we gathered photometry data. The spectrophotometry from the spectra from the HSA default product (collected in mid-2014) are roughly a factor of 4 lower than the photometry. The spectrophotometry from our archive (benefiting from the semi-extended source correction processing), shown in blue, agrees significantly better with the actual photometry. Separate fits to the HSA product spectrophotometry and our product spectrophotometry have similar slopes, which do not match the line of equality. The increasing deviation at faint sources is therefore not caused by the semi-extended correction but derives from the uncorrected spectral data. Note that the scatter in the fit residual is nearly identical—0.19 for HSA products and 0.18 for CDF products.

We also find improved agreement with previous ground-based submillimeter data. We compared the filter-convolved spectrophotometry from this archive with SPIRE photometry for almost all SPIRE sources in this archive and SCUBA/SHARC-II total flux for the sources from Shirley et al. (2000), Young et al. (2006), and Wu et al. (2007). The mean ratio of spectrophotometry from this archive over the flux measured by SCUBA/SHARC-II is 1.19, while the mean ratio measured from the spectrophotometry from the HSA is only 0.38. The scatter in the residual subtracted with the fitted line is 0.11 for HSA products and 0.09 for CDF products.

The semi-extended source correction has greatly improved the SPIRE spectrophotometry, but it has introduced an offset between the longest wavelength in the PACS data and the shortest wavelength in the SPIRE data, which usually has more emission than the extrapolated PACS data (Figure 9). This problem arises from the fact that the semi-extended source corrector assumes a source size that is constant with wavelength and because no background subtraction was performed. In bright extended sources, the mismatch is systematic as noted above. In fainter sources (those with  $200\text{ }\mu\text{m}$  intensity  $\lesssim 25\text{ Jy}$ , the SPIRE flux exceeds the PACS flux by a factor of three on average. The protostars in our sample are typically resolved (marginally) by SPIRE, and their spatial extent increases with wavelength. As the corrector assumes a source model that is independent of wavelength, it overpredicts the flux at short SPIRE wavelengths; thus the SPIRE flux for  $\lambda \lesssim 300\text{ }\mu\text{m}$  is too high for extended sources. Improving this result requires knowledge of source intensity distribution as a function of wavelength. We apply a 3D radiative transfer model to explore this issue for one protostar in an upcoming paper (Y.-L. Yang et al. 2016, in preparation), but, lacking models for all sources, our archival products cannot account for this effect. The SPIRE spectrum should be considered an upper limit to the true flux density at the shortest wavelengths.

#### 4. AUTOMATED LINE-FITTING

We use an automated emission line fitting process (available at GitHub<sup>11</sup>) that tries to fit lines from a pre-existing database of laboratory wavelengths, identifies the threshold for detection, then generates tables of line flux, width, centroid, and uncertainties for every detected line, along with an upper limit to the flux for every undetected line for all PACS and SPIRE

spectra in the sample. This information is then combined with spatial information for each pixel to produce contour maps including all spatial positions where significant detections are found. The line-fitting algorithm uses `mpfit`, a Levenberg–Marquardt nonlinear least squares minimization (Markwardt 2009), to determine emission line properties. After producing a line detection database, we test the integrity of the line fits to better characterize the S/N, decouple any blended line, and produce easily searchable products for further science applications. The automated results have been spot checked by eye but should be used with caution. In particular, lines that are distributed very differently in space from the continuum emission, or sources in complex regions will need special consideration. The detailed procedures are described in the following sections and an overview of the process is shown in Figure 8.

##### 4.1. Line List

A comprehensive and pre-selected line list is used to supply initial fit parameters for the automated routine. We require an expected line list to restrict our line fitting to specific regions of the spectrum, pre-select line-free continuum regions, and identify the lines after fitting. For this data set, we verified that there were no significant unidentified lines. If the input spectrum contains a line that is not included in our list, one can easily check whether every significant feature has been extracted from the spectrum: any line not included in the linelist will then appear in the residual spectrum (see Section 5). The line list includes lines of CO,  $^{13}\text{CO}$ ,  $\text{H}_2\text{O}$ , OH,  $\text{HCO}^+$ ,  $\text{CH}^+$ , and atomic fine-structure transitions in the wavelength range of  $55\text{--}670\text{ }\mu\text{m}$  (Tables 2–6). Table 7 lists potentially blended lines that are fitted with double Gaussians (see Section 4.4). Two  $\text{CH}^+$  lines,  $\text{CH}^+ J = 4 \rightarrow 3$  and  $\text{CH}^+ J = 2 \rightarrow 1$ , were excluded because they are heavily blended with nearby potentially strong water lines.

The laboratory data for each line were collected from the Leiden Atomic and Molecular Database (LAMDA; Schöier et al. 2005) and the Cologne Database for Molecular Spectroscopy (CDMS; Müller et al. 2005). However, the CO  $J = 48 \rightarrow 47$  to CO  $J = 41 \rightarrow 40$  lines were not included in LAMDA until recently; thus we calculated the frequency and Einstein-A coefficient using a method from Authier et al. (1993) and the model of the dipole matrix element in Goorvitch (1994). An updated CO extrapolation added to LAMDA (D. Neufeld 2016, in preparation) agrees with our calculations. We use slightly different line centroids of OH lines, adopted from Wampfler et al. (2013). The only difference is the line centroid of OH  $2\Pi_{1/2,3/2}^+ - 2\Pi_{1/2,1/2}^-$ ; we use  $163.12\text{ }\mu\text{m}$  instead of the value of  $163.019\text{ }\mu\text{m}$  from LAMDA. We use only subsets of the line list within the wavelength range of the observations for each specific source. Finally, we note that [N II] 122 and 205  $\mu\text{m}$  do not appear in the LAMDA database, and there is a discrepancy between the centroid reported in the ISO-LWS line list (taken from the SMART data reduction package, Higdon et al. 2004) and the line list from Peter van Hoof (<http://www.pa.uky.edu/~peter/atomic/>). We used the line centroids from the ISO line list as initial guess, but allowed the line centroids to vary up to  $\pm 2$  spectral resolution to determine better values. The averaged fitted line centroids of two [N II] lines from all detections with  $S/N > 10$  are 121.911 and 205.170  $\mu\text{m}$ . In Table 6, we report the mean values and the standard deviation of the mean of two

<sup>11</sup> [https://github.com/yaolun/Her\\_line\\_fit](https://github.com/yaolun/Her_line_fit)

**Table 1**  
Archive Sources

Source	Other Name	PACS OBSIDs	SPIRE OBSID	R.A.	Decl.	Prog.	Jitter Corr.	SPIRE ID
AB Aur	...	1342217842, 1342217843	...	04 <sup>h</sup> 55 <sup>m</sup> 45 <sup>s</sup> .8	+30 <sup>d</sup> 33 <sup>m</sup> 04 <sup>s</sup> .3	D	x	...
AS 205	...	1342215737, 1342215738	...	16 <sup>h</sup> 11 <sup>m</sup> 31 <sup>s</sup> .4	-18 <sup>d</sup> 38 <sup>m</sup> 26 <sup>s</sup>	D	x	...
B1-a	...	1342216182, 1342216183	1342249475	03 <sup>h</sup> 33 <sup>m</sup> 16 <sup>s</sup> .7	+31 <sup>d</sup> 07 <sup>m</sup> 55 <sup>s</sup> .2	D, C	x	x
B1-c	...	1342216213, 1342216214	1342249476	03 <sup>h</sup> 33 <sup>m</sup> 17 <sup>s</sup> .9	+31 <sup>d</sup> 09 <sup>m</sup> 31 <sup>s</sup> .9	D, C	x	x
B335	...	1342208889, 1342208888	1342253652	19 <sup>h</sup> 37 <sup>m</sup> 00 <sup>s</sup> .9	+07 <sup>d</sup> 34 <sup>m</sup> 09 <sup>s</sup> .7	D, C	x	x
BHR 71	...	1342212230, 1342212231	1342248249	12 <sup>h</sup> 01 <sup>m</sup> 36 <sup>s</sup> .3	-65 <sup>d</sup> 08 <sup>m</sup> 53 <sup>s</sup> .0	D, C	x	x
Ced 110-IRS4	...	...	1342248246	11 <sup>h</sup> 06 <sup>m</sup> 47 <sup>s</sup> .0	-77 <sup>d</sup> 22 <sup>m</sup> 32 <sup>s</sup> .4	C	...	x
DG Tau	...	1342225730, 1342225731	...	04 <sup>h</sup> 27 <sup>m</sup> 04 <sup>s</sup> .7	+26 <sup>d</sup> 06 <sup>m</sup> 16 <sup>s</sup>	D	x	...
DK Cha	IRAS 12496–7650	1342188039, 1342188040	1342254037	12 <sup>h</sup> 53 <sup>m</sup> 17 <sup>s</sup> .2	-77 <sup>d</sup> 07 <sup>m</sup> 10 <sup>s</sup> .7	D, C	x	x
EC 82	[EC92] 82	1342192975, 1342219435	...	18 <sup>h</sup> 29 <sup>m</sup> 56 <sup>s</sup> .9	+01 <sup>d</sup> 14 <sup>m</sup> 47 <sup>s</sup>	D	...	...
Elias 29	...	1342228519, 1342228520	...	16 <sup>h</sup> 27 <sup>m</sup> 09 <sup>s</sup> .4	-24 <sup>d</sup> 37 <sup>m</sup> 18 <sup>s</sup> .6	D	x	x
FU Ori	...	1342250907, 1342250908	1342230412	05 <sup>h</sup> 45 <sup>m</sup> 22 <sup>s</sup> .4	+09 <sup>d</sup> 04 <sup>m</sup> 12 <sup>s</sup>	F	x	x
GSS 30-IRS1	...	1342215678, 1342215679	1342251286	16 <sup>h</sup> 26 <sup>m</sup> 21 <sup>s</sup> .4	-24 <sup>d</sup> 23 <sup>m</sup> 04 <sup>s</sup> .3	D, C	x	x
HD 100453	...	1342211695, 1342211696	...	11 <sup>h</sup> 33 <sup>m</sup> 05 <sup>s</sup> .6	-54 <sup>d</sup> 19 <sup>m</sup> 29 <sup>s</sup>	D	x	...
HD 100546	...	1342188037, 1342188038	...	11 <sup>h</sup> 33 <sup>m</sup> 25 <sup>s</sup> .4	-70 <sup>d</sup> 11 <sup>m</sup> 41 <sup>s</sup>	D	x	...
HD 104237	...	1342207819, 1342207820	...	12 <sup>h</sup> 00 <sup>m</sup> 05 <sup>s</sup> .1	-78 <sup>d</sup> 11 <sup>m</sup> 35 <sup>s</sup>	D	x	...
HD 135344	...	1342213921, 1342213922	...	15 <sup>h</sup> 15 <sup>m</sup> 49 <sup>s</sup> .0	-37 <sup>d</sup> 08 <sup>m</sup> 56 <sup>s</sup>	D	x	...
HD 139614	...	1342215683, 1342215684	...	15 <sup>h</sup> 40 <sup>m</sup> 46 <sup>s</sup> .4	-42 <sup>d</sup> 29 <sup>m</sup> 54 <sup>s</sup>	D	x	...
HD 141569	...	1342213913	...	15 <sup>h</sup> 49 <sup>m</sup> 57 <sup>s</sup> .8	-03 <sup>d</sup> 55 <sup>m</sup> 16 <sup>s</sup>	D	x	...
HD 142527	...	1342216174, 1342216175	...	15 <sup>h</sup> 56 <sup>m</sup> 41 <sup>s</sup> .9	-42 <sup>d</sup> 19 <sup>m</sup> 23 <sup>s</sup>	D	x	...
HD 142666	...	1342213916	...	15 <sup>h</sup> 56 <sup>m</sup> 40 <sup>s</sup> .0	-22 <sup>d</sup> 01 <sup>m</sup> 40 <sup>s</sup>	D	...	...
HD 144432	...	1342213919	...	16 <sup>h</sup> 06 <sup>m</sup> 58 <sup>s</sup> .0	-27 <sup>d</sup> 43 <sup>m</sup> 10 <sup>s</sup>	D	x	...
HD 144668	...	1342215641, 1342215642	...	16 <sup>h</sup> 08 <sup>m</sup> 34 <sup>s</sup> .3	-39 <sup>d</sup> 06 <sup>m</sup> 18 <sup>s</sup>	D	x	...
HD 150193	...	1342227068	...	16 <sup>h</sup> 40 <sup>m</sup> 17 <sup>s</sup> .9	-23 <sup>d</sup> 53 <sup>m</sup> 45 <sup>s</sup>	D	x	...
HD 163296	...	1342217819, 1342217820	...	17 <sup>h</sup> 56 <sup>m</sup> 21 <sup>s</sup> .3	-21 <sup>d</sup> 57 <sup>m</sup> 22 <sup>s</sup>	D	x	...
HD 169142	...	1342206987, 1342206988	...	18 <sup>h</sup> 24 <sup>m</sup> 29 <sup>s</sup> .8	-29 <sup>d</sup> 46 <sup>m</sup> 49 <sup>s</sup>	D	x	...
HD 179218	...	1342208884, 1342208885	...	19 <sup>h</sup> 11 <sup>m</sup> 11 <sup>s</sup> .3	+15 <sup>d</sup> 47 <sup>m</sup> 16 <sup>s</sup>	D	x	...
HD 203024	...	1342206975	...	21 <sup>h</sup> 16 <sup>m</sup> 03 <sup>s</sup> .0	+68 <sup>d</sup> 54 <sup>m</sup> 52 <sup>s</sup>	D	...	...
HD 245906	...	1342228528	...	05 <sup>h</sup> 39 <sup>m</sup> 30 <sup>s</sup> .5	+26 <sup>d</sup> 19 <sup>m</sup> 55 <sup>s</sup>	D	...	...
HD 35187	...	1342217846	...	05 <sup>h</sup> 24 <sup>m</sup> 01 <sup>s</sup> .2	+24 <sup>d</sup> 57 <sup>m</sup> 38 <sup>s</sup>	D	x	...
HD 36112	...	1342228247, 1342228248	...	05 <sup>h</sup> 30 <sup>m</sup> 27 <sup>s</sup> .5	+25 <sup>d</sup> 19 <sup>m</sup> 57 <sup>s</sup>	D	x	...
HD 38120	...	1342226212, 1342226213	...	05 <sup>h</sup> 43 <sup>m</sup> 11 <sup>s</sup> .9	-04 <sup>d</sup> 59 <sup>m</sup> 50 <sup>s</sup>	D	x	...
HD 50138	...	1342206991, 1342206992	...	06 <sup>h</sup> 51 <sup>m</sup> 33 <sup>s</sup> .4	-06 <sup>d</sup> 57 <sup>m</sup> 59 <sup>s</sup>	D	x	...
HD 97048	...	1342199412, 1342199413	...	11 <sup>h</sup> 08 <sup>m</sup> 03 <sup>s</sup> .3	-77 <sup>d</sup> 39 <sup>m</sup> 18 <sup>s</sup>	D	x	...
HD 98922	...	1342210385	...	11 <sup>h</sup> 22 <sup>m</sup> 31 <sup>s</sup> .7	-53 <sup>d</sup> 22 <sup>m</sup> 12 <sup>s</sup>	D	...	...
HH 100	...	...	1342252897	19 <sup>h</sup> 01 <sup>m</sup> 49 <sup>s</sup> .1	-36 <sup>d</sup> 58 <sup>m</sup> 16 <sup>s</sup> .0	C	...	...
HH 46	...	...	1342245084	08 <sup>h</sup> 25 <sup>m</sup> 43 <sup>s</sup> .9	-51 <sup>d</sup> 00 <sup>m</sup> 36 <sup>s</sup> .0	C	...	x
HT Lup	...	1342213920	...	15 <sup>h</sup> 45 <sup>m</sup> 12 <sup>s</sup> .9	-34 <sup>d</sup> 17 <sup>m</sup> 31 <sup>s</sup>	D	...	...
IRAM 04191+1522	...	1342216654, 1342216655	...	04 <sup>h</sup> 21 <sup>m</sup> 56 <sup>s</sup> .9	+15 <sup>d</sup> 29 <sup>m</sup> 45 <sup>s</sup> .9	D	...	...
IRAS 03245+3002	L1455-IRS1	1342214677, 1342214676	1342249053	03 <sup>h</sup> 27 <sup>m</sup> 39 <sup>s</sup> .1	+30 <sup>d</sup> 13 <sup>m</sup> 03 <sup>s</sup> .1	D, C	x	x
IRAS 03301+3111	Perseus Bolo76	1342215668, 1342216181	1342249477	03 <sup>h</sup> 33 <sup>m</sup> 12 <sup>s</sup> .8	+31 <sup>d</sup> 21 <sup>m</sup> 24 <sup>s</sup> .2	D, C	x	x
IRAS 15398–3359	B228	...	1342250515	15 <sup>h</sup> 43 <sup>m</sup> 01 <sup>s</sup> .3	-34 <sup>d</sup> 09 <sup>m</sup> 15 <sup>s</sup> .0	C	...	x
IRS 46/IRS44	Oph-IRS44/46	1342228474, 1342228475	1342251289	16 <sup>h</sup> 27 <sup>m</sup> 29 <sup>s</sup> .4	-24 <sup>d</sup> 39 <sup>m</sup> 16 <sup>s</sup> .1	D, C	...	...
IRS 48	Oph-IRS48	1342227069, 1342227070	...	16 <sup>h</sup> 27 <sup>m</sup> 37 <sup>s</sup> .2	-24 <sup>d</sup> 30 <sup>m</sup> 35 <sup>s</sup>	D	x	...
IRS 63	Oph-IRS63	1342228473, 1342228472	...	16 <sup>h</sup> 31 <sup>m</sup> 35 <sup>s</sup> .6	-24 <sup>d</sup> 01 <sup>m</sup> 29 <sup>s</sup> .3	D	x	...
L1014	...	1342208911, 1342208912	1342245857	21 <sup>h</sup> 24 <sup>m</sup> 07 <sup>s</sup> .5	+49 <sup>d</sup> 59 <sup>m</sup> 09 <sup>s</sup> .0	D, C	...	x
L1157	...	1342208909, 1342208908	1342247625	20 <sup>h</sup> 39 <sup>m</sup> 06 <sup>s</sup> .3	+68 <sup>d</sup> 02 <sup>m</sup> 16 <sup>s</sup> .0	D, C	x	x
L1448-MM	...	1342213683, 1342214675	...	03 <sup>h</sup> 25 <sup>m</sup> 38 <sup>s</sup> .9	+30 <sup>d</sup> 44 <sup>m</sup> 05 <sup>s</sup> .4	D	x	x

**Table 1**  
(Continued)

Source	Other Name	PACS OBSIDs	SPIRE OBSID	R.A.	Decl.	Prog.	Jitter Corr.	SPIRE 1D
L1455-IRS3	IRAS 03249+2957	1342204122, 1342204123	1342249474	03 <sup>h</sup> 28 <sup>m</sup> 00 <sup>s</sup> .4	+30 <sup>d</sup> 08 <sup>m</sup> 01 <sup>s</sup> .3	D, C	...	x
L1489	IRAS 04016+2610	1342216216, 1342216215	...	04 <sup>h</sup> 04 <sup>m</sup> 42 <sup>s</sup> .9	+26 <sup>d</sup> 18 <sup>m</sup> 56 <sup>s</sup> .3	D	x	...
L1527	IRAS 04368+2557	1342192981, 1342192982	...	04 <sup>h</sup> 39 <sup>m</sup> 53 <sup>s</sup> .9	+26 <sup>d</sup> 03 <sup>m</sup> 09 <sup>s</sup> .8	D	x	...
L1551-IRS5	...	1342192805, 1342229711	1342249470	04 <sup>h</sup> 31 <sup>m</sup> 34 <sup>s</sup> .1	+18 <sup>d</sup> 08 <sup>m</sup> 04 <sup>s</sup> .9	D, C	x	x
L483	IRAS 18140-0440	...	1342253649	18 <sup>h</sup> 17 <sup>m</sup> 29 <sup>s</sup> .9	-04 <sup>d</sup> 39 <sup>m</sup> 39 <sup>s</sup> .5	C	...	x
L723-MM	...	...	1342245094	19 <sup>h</sup> 17 <sup>m</sup> 53 <sup>s</sup> .7	+19 <sup>d</sup> 12 <sup>m</sup> 20 <sup>s</sup> .0	C	...	x
RCrA-IRS5A	...	1342207806, 1342207805	1342253646	19 <sup>h</sup> 01 <sup>m</sup> 48 <sup>s</sup> .1	-36 <sup>d</sup> 57 <sup>m</sup> 22 <sup>s</sup> .7	D, C	...	x
RCrA-IRS7B	...	1342207807, 1342207808	1342242620	19 <sup>h</sup> 01 <sup>m</sup> 56 <sup>s</sup> .4	-36 <sup>d</sup> 57 <sup>m</sup> 28 <sup>s</sup> .3	D, C	x	x
RCrA-IRS7C	...	1342206990, 1342206989	1342242621	19 <sup>h</sup> 01 <sup>m</sup> 55 <sup>s</sup> .3	-36 <sup>d</sup> 57 <sup>m</sup> 17 <sup>s</sup> .0	D, C	...	x
RNO 90	...	1342228206	...	16 <sup>h</sup> 34 <sup>m</sup> 09 <sup>s</sup> .2	-15 <sup>d</sup> 48 <sup>m</sup> 17 <sup>s</sup>	D	x	...
RNO 91	...	...	1342251285	16 <sup>h</sup> 34 <sup>m</sup> 29 <sup>s</sup> .3	-15 <sup>d</sup> 47 <sup>m</sup> 01 <sup>s</sup> .4	C	...	x
RU Lup	...	1342215682	...	15 <sup>h</sup> 56 <sup>m</sup> 42 <sup>s</sup> .3	-37 <sup>d</sup> 49 <sup>m</sup> 16 <sup>s</sup>	D	x	...
RY Lup	...	1342216171	...	15 <sup>h</sup> 59 <sup>m</sup> 28 <sup>s</sup> .4	-40 <sup>d</sup> 21 <sup>m</sup> 51 <sup>s</sup>	D	x	...
S Cra	...	1342207809, 1342207810	...	19 <sup>h</sup> 01 <sup>m</sup> 08 <sup>s</sup> .6	-36 <sup>d</sup> 57 <sup>m</sup> 20 <sup>s</sup>	D	x	...
Serpens-SMM3	...	1342193216, 1342193214	...	18 <sup>h</sup> 29 <sup>m</sup> 59 <sup>s</sup> .3	+01 <sup>d</sup> 14 <sup>m</sup> 01 <sup>s</sup> .7	D	x	...
Serpens-SMM4	...	1342193217, 1342193215	...	18 <sup>h</sup> 29 <sup>m</sup> 56 <sup>s</sup> .7	+01 <sup>d</sup> 13 <sup>m</sup> 17 <sup>s</sup> .2	D	...	...
SR 21	...	1342227209, 1342227210	...	16 <sup>h</sup> 27 <sup>m</sup> 10 <sup>s</sup> .3	-24 <sup>d</sup> 19 <sup>m</sup> 13 <sup>s</sup>	D	x	...
TMC 1A	IRAS 04362+2535	1342192987, 1342192988	1342250510	04 <sup>h</sup> 39 <sup>m</sup> 35 <sup>s</sup> .0	+25 <sup>d</sup> 41 <sup>m</sup> 45 <sup>s</sup> .5	D, C	x	x
TMC 1	IRAS 04381+2540	1342225803, 1342225804	1342250512	04 <sup>h</sup> 41 <sup>m</sup> 12 <sup>s</sup> .7	+25 <sup>d</sup> 46 <sup>m</sup> 35 <sup>s</sup> .9	D, C	x	x
TMR 1	IRAS 04361+2547	1342192985, 1342192986	1342250509	04 <sup>h</sup> 39 <sup>m</sup> 13 <sup>s</sup> .9	+25 <sup>d</sup> 53 <sup>m</sup> 20 <sup>s</sup> .6	D, C	x	x
V1057 Cyg	...	1342235853, 1342235852	1342221695	20 <sup>h</sup> 58 <sup>m</sup> 53 <sup>s</sup> .7	+44 <sup>d</sup> 15 <sup>m</sup> 29 <sup>s</sup>	F	x	x
V1331 Cyg	...	1342233446, 1342233445	1342221694	21 <sup>h</sup> 01 <sup>m</sup> 09 <sup>s</sup> .2	+50 <sup>d</sup> 21 <sup>m</sup> 45 <sup>s</sup>	F	x	x
V1515 Cyg	...	1342235691, 1342235690	1342221685	20 <sup>h</sup> 23 <sup>m</sup> 48 <sup>s</sup> .0	+42 <sup>d</sup> 12 <sup>m</sup> 26 <sup>s</sup>	F	x	x
V1735 Cyg	Elias 1-12	1342235849, 1342235848	1342219560	21 <sup>h</sup> 47 <sup>m</sup> 20 <sup>s</sup> .7	+47 <sup>d</sup> 32 <sup>m</sup> 04 <sup>s</sup>	F	x	...
VLA 1623-243	...	1342213918, 1342213917	1342251287	16 <sup>h</sup> 26 <sup>m</sup> 26 <sup>s</sup> .4	-24 <sup>d</sup> 24 <sup>m</sup> 30 <sup>s</sup> .0	D, C	x	x
WL 12	...	1342228187, 1342228188	1342251290	16 <sup>h</sup> 26 <sup>m</sup> 44 <sup>s</sup> .2	-24 <sup>d</sup> 34 <sup>m</sup> 48 <sup>s</sup> .4	D, C	x	x

**Note.** Contents of the archive organized by source. The “Prog.” column refers to the first program in which the source was observed, where D = DIGIT, F = FOOSH, and C = COPS. The “Jitter Corr.” column indicates the accessibility of the Jitter corrected data. Sources with an “x” in this column use the Jitter-corrected products. The “SPIRE 1D” column indicates the accessibility of SPIRE extended calibrated 1D spectra.

**Table 2**  
Line List for Single Gaussian Fitting: o-H<sub>2</sub>O

Wavelength ( $\mu\text{m}$ )	Line Name	Wavelength ( $\mu\text{m}$ )	Line Name
55.13238	o-H <sub>2</sub> O 8 <sub>27</sub> –7 <sub>16</sub>	55.84108	o-H <sub>2</sub> O 10 <sub>29</sub> –10 <sub>110</sub>
56.81777	o-H <sub>2</sub> O 9 <sub>09</sub> –8 <sub>18</sub>	57.39511	o-H <sub>2</sub> O 7 <sub>52</sub> –8 <sub>27</sub>
58.70051	o-H <sub>2</sub> O 4 <sub>32</sub> –3 <sub>21</sub>	61.31782	o-H <sub>2</sub> O 5 <sub>41</sub> –6 <sub>16</sub>
62.92979	o-H <sub>2</sub> O 9 <sub>18</sub> –9 <sub>09</sub>	63.32514	o-H <sub>2</sub> O 8 <sub>18</sub> –7 <sub>07</sub>
63.91602	o-H <sub>2</sub> O 6 <sub>61</sub> –6 <sub>52</sub>	63.95796	o-H <sub>2</sub> O 7 <sub>61</sub> –7 <sub>52</sub>
65.16779	o-H <sub>2</sub> O 6 <sub>25</sub> –5 <sub>14</sub>	66.09434	o-H <sub>2</sub> O 7 <sub>16</sub> –6 <sub>25</sub>
66.43937	o-H <sub>2</sub> O 3 <sub>30</sub> –2 <sub>21</sub>	67.27067	o-H <sub>2</sub> O 3 <sub>30</sub> –3 <sub>03</sub>
70.70435	o-H <sub>2</sub> O 8 <sub>27</sub> –8 <sub>18</sub>	71.94881	o-H <sub>2</sub> O 7 <sub>07</sub> –6 <sub>16</sub>
74.94690	o-H <sub>2</sub> O 7 <sub>25</sub> –6 <sub>34</sub>	75.38257	o-H <sub>2</sub> O 3 <sub>21</sub> –2 <sub>12</sub>
75.49740	o-H <sub>2</sub> O 8 <sub>34</sub> –8 <sub>45</sub>	75.83188	o-H <sub>2</sub> O 6 <sub>52</sub> –6 <sub>43</sub>
75.91180	o-H <sub>2</sub> O 5 <sub>50</sub> –5 <sub>41</sub>	77.76345	o-H <sub>2</sub> O 7 <sub>52</sub> –7 <sub>43</sub>
78.74431	o-H <sub>2</sub> O 4 <sub>23</sub> –3 <sub>12</sub>	81.40747	o-H <sub>2</sub> O 9 <sub>27</sub> –9 <sub>18</sub>
82.03351	o-H <sub>2</sub> O 6 <sub>16</sub> –5 <sub>05</sub>	82.97879	o-H <sub>2</sub> O 8 <sub>36</sub> –8 <sub>27</sub>
84.76907	o-H <sub>2</sub> O 7 <sub>16</sub> –7 <sub>07</sub>	85.77088	o-H <sub>2</sub> O 8 <sub>45</sub> –8 <sub>36</sub>
92.81312	o-H <sub>2</sub> O 6 <sub>43</sub> –6 <sub>34</sub>	94.64643	o-H <sub>2</sub> O 6 <sub>25</sub> –6 <sub>16</sub>
94.70758	o-H <sub>2</sub> O 4 <sub>41</sub> –4 <sub>32</sub>	104.09629	o-H <sub>2</sub> O 6 <sub>34</sub> –6 <sub>25</sub>
108.07588	o-H <sub>2</sub> O 2 <sub>21</sub> –1 <sub>10</sub>	112.51342	o-H <sub>2</sub> O 7 <sub>43</sub> –7 <sub>34</sub>
112.80576	o-H <sub>2</sub> O 4 <sub>41</sub> –5 <sub>14</sub>	113.54021	o-H <sub>2</sub> O 4 <sub>14</sub> –3 <sub>03</sub>
114.45656	o-H <sub>2</sub> O 9 <sub>27</sub> –10 <sub>110</sub>	116.35288	o-H <sub>2</sub> O 8 <sub>36</sub> –9 <sub>09</sub>
116.78196	o-H <sub>2</sub> O 7 <sub>34</sub> –6 <sub>43</sub>	121.72477	o-H <sub>2</sub> O 4 <sub>32</sub> –4 <sub>23</sub>
123.46352	o-H <sub>2</sub> O 9 <sub>36</sub> –9 <sub>27</sub>	127.88735	o-H <sub>2</sub> O 7 <sub>25</sub> –7 <sub>16</sub>
129.34220	o-H <sub>2</sub> O 9 <sub>45</sub> –9 <sub>36</sub>	132.41173	o-H <sub>2</sub> O 4 <sub>23</sub> –4 <sub>14</sub>
133.55242	o-H <sub>2</sub> O 8 <sub>36</sub> –7 <sub>43</sub>	134.93863	o-H <sub>2</sub> O 5 <sub>14</sub> –5 <sub>05</sub>
136.49943	o-H <sub>2</sub> O 3 <sub>30</sub> –3 <sub>21</sub>	156.26908	o-H <sub>2</sub> O 5 <sub>23</sub> –4 <sub>32</sub>
159.05453	o-H <sub>2</sub> O 8 <sub>45</sub> –7 <sub>52</sub>	159.40427	o-H <sub>2</sub> O 6 <sub>34</sub> –7 <sub>07</sub>
160.51410	o-H <sub>2</sub> O 5 <sub>32</sub> –5 <sub>23</sub>	166.81885	o-H <sub>2</sub> O 7 <sub>34</sub> –7 <sub>25</sub>
174.63028	o-H <sub>2</sub> O 3 <sub>03</sub> –2 <sub>12</sub>	174.92441	o-H <sub>2</sub> O 4 <sub>32</sub> –5 <sub>05</sub>
179.53118	o-H <sub>2</sub> O 2 <sub>12</sub> –1 <sub>01</sub>	180.49281	o-H <sub>2</sub> O 2 <sub>21</sub> –2 <sub>12</sub>
187.81488	o-H <sub>2</sub> O 8 <sub>54</sub> –9 <sub>27</sub>	212.53093	o-H <sub>2</sub> O 5 <sub>23</sub> –5 <sub>14</sub>
226.76647	o-H <sub>2</sub> O 6 <sub>25</sub> –5 <sub>32</sub>	229.21129	o-H <sub>2</sub> O 8 <sub>45</sub> –9 <sub>18</sub>
231.25379	o-H <sub>2</sub> O 8 <sub>27</sub> –7 <sub>34</sub>	234.53645	o-H <sub>2</sub> O 7 <sub>43</sub> –6 <sub>52</sub>
256.59928	o-H <sub>2</sub> O 8 <sub>54</sub> –7 <sub>61</sub>	257.80114	o-H <sub>2</sub> O 3 <sub>21</sub> –3 <sub>12</sub>
258.82221	o-H <sub>2</sub> O 6 <sub>34</sub> –5 <sub>41</sub>	259.98875	o-H <sub>2</sub> O 3 <sub>12</sub> –2 <sub>21</sub>
261.46379	o-H <sub>2</sub> O 7 <sub>25</sub> –8 <sub>18</sub>	273.19988	o-H <sub>2</sub> O 3 <sub>12</sub> –3 <sub>03</sub>
483.00214	o-H <sub>2</sub> O 5 <sub>32</sub> –4 <sub>41</sub>	538.30236	o-H <sub>2</sub> O 1 <sub>10</sub> –1 <sub>01</sub>

[N II] lines. Figure 6 shows the detected [N II] 122  $\mu\text{m}$  and [N II] 205  $\mu\text{m}$  lines found in this archive.

#### 4.2. Baseline Selection and Fitting

Before fitting each line, we select a nearby spectral region without line emission, from wavelengths near the theoretical line centroid (hereinafter referred as “line-region”) and use this region for baseline fitting. The baseline fitting region is 10 times the spectral resolution at the wavelength of the line centroid. However, some of these wavelengths may include other emission lines. Thus we use only line-free wavelengths (determined from our previously constructed line list) until we have accumulated 5 times the spectral resolution, both blue-ward and red-ward of the line centroid. Then, we fit the selected baseline region using a second order polynomial. Once we obtain a well-constrained baseline, we subtract the baseline from the identified wavelength region. This continuum-subtracted spectrum is then used for line-fitting.

#### 4.3. Line Selection and Fitting

We begin with the baseline-subtracted spectrum. The next step is to extract the line profile, using a Gaussian model.

**Table 3**  
Line List for Single Gaussian Fitting: p-H<sub>2</sub>O

Wavelength ( $\mu\text{m}$ )	Line Name	Wavelength ( $\mu\text{m}$ )	Line Name
55.85970	p-H <sub>2</sub> O 6 <sub>51</sub> –7 <sub>26</sub>	55.98480	p-H <sub>2</sub> O 7 <sub>71</sub> –7 <sub>62</sub>
56.02824	p-H <sub>2</sub> O 10 <sub>19</sub> –10 <sub>010</sub>	56.32640	p-H <sub>2</sub> O 4 <sub>31</sub> –3 <sub>22</sub>
56.77240	p-H <sub>2</sub> O 9 <sub>19</sub> –8 <sub>08</sub>	57.63798	p-H <sub>2</sub> O 4 <sub>22</sub> –3 <sub>13</sub>
57.71080	p-H <sub>2</sub> O 8 <sub>17</sub> –7 <sub>26</sub>	58.37824	p-H <sub>2</sub> O 6 <sub>42</sub> –7 <sub>17</sub>
59.98863	p-H <sub>2</sub> O 7 <sub>26</sub> –6 <sub>15</sub>	60.16365	p-H <sub>2</sub> O 8 <sub>26</sub> –7 <sub>35</sub>
60.23082	p-H <sub>2</sub> O 7 <sub>62</sub> –8 <sub>35</sub>	61.81016	p-H <sub>2</sub> O 4 <sub>31</sub> –4 <sub>04</sub>
61.91772	p-H <sub>2</sub> O 4 <sub>40</sub> –5 <sub>15</sub>	62.43311	p-H <sub>2</sub> O 9 <sub>28</sub> –9 <sub>19</sub>
63.45961	p-H <sub>2</sub> O 8 <sub>08</sub> –7 <sub>17</sub>	63.88177	p-H <sub>2</sub> O 7 <sub>62</sub> –7 <sub>53</sub>
67.09082	p-H <sub>2</sub> O 3 <sub>31</sub> –2 <sub>20</sub>	71.06907	p-H <sub>2</sub> O 5 <sub>24</sub> –4 <sub>13</sub>
71.54146	p-H <sub>2</sub> O 7 <sub>17</sub> –6 <sub>06</sub>	71.78955	p-H <sub>2</sub> O 5 <sub>51</sub> –6 <sub>24</sub>
72.03407	p-H <sub>2</sub> O 8 <sub>17</sub> –8 <sub>08</sub>	73.61471	p-H <sub>2</sub> O 9 <sub>37</sub> –9 <sub>28</sub>
75.78324	p-H <sub>2</sub> O 5 <sub>51</sub> –5 <sub>42</sub>	75.81532	p-H <sub>2</sub> O 7 <sub>53</sub> –7 <sub>44</sub>
76.42386	p-H <sub>2</sub> O 6 <sub>51</sub> –6 <sub>42</sub>	78.93042	p-H <sub>2</sub> O 6 <sub>15</sub> –5 <sub>24</sub>
80.22431	p-H <sub>2</sub> O 9 <sub>46</sub> –9 <sub>37</sub>	80.55884	p-H <sub>2</sub> O 8 <sub>53</sub> –8 <sub>44</sub>
81.21765	p-H <sub>2</sub> O 7 <sub>26</sub> –7 <sub>17</sub>	81.69220	p-H <sub>2</sub> O 8 <sub>35</sub> –7 <sub>44</sub>
83.28606	p-H <sub>2</sub> O 6 <sub>06</sub> –5 <sub>15</sub>	89.99061	p-H <sub>2</sub> O 3 <sub>22</sub> –2 <sub>11</sub>
90.05205	p-H <sub>2</sub> O 7 <sub>44</sub> –7 <sub>35</sub>	94.21193	p-H <sub>2</sub> O 5 <sub>42</sub> –5 <sub>33</sub>
103.91892	p-H <sub>2</sub> O 6 <sub>42</sub> –6 <sub>33</sub>	103.94278	p-H <sub>2</sub> O 6 <sub>15</sub> –6 <sub>06</sub>
111.63078	p-H <sub>2</sub> O 5 <sub>24</sub> –5 <sub>15</sub>	113.95081	p-H <sub>2</sub> O 5 <sub>33</sub> –5 <sub>24</sub>
117.68692	p-H <sub>2</sub> O 9 <sub>46</sub> –8 <sub>53</sub>	118.40826	p-H <sub>2</sub> O 9 <sub>37</sub> –8 <sub>44</sub>
122.52519	p-H <sub>2</sub> O 8 <sub>44</sub> –8 <sub>35</sub>	125.35683	p-H <sub>2</sub> O 4 <sub>04</sub> –3 <sub>13</sub>
126.71711	p-H <sub>2</sub> O 3 <sub>31</sub> –3 <sub>22</sub>	130.32199	p-H <sub>2</sub> O 7 <sub>53</sub> –8 <sub>26</sub>
137.68652	p-H <sub>2</sub> O 7 <sub>35</sub> –8 <sub>08</sub>	138.53127	p-H <sub>2</sub> O 3 <sub>13</sub> –2 <sub>02</sub>
138.64412	p-H <sub>2</sub> O 8 <sub>44</sub> –7 <sub>53</sub>	144.52144	p-H <sub>2</sub> O 4 <sub>13</sub> –3 <sub>22</sub>
146.92643	p-H <sub>2</sub> O 4 <sub>31</sub> –4 <sub>22</sub>	148.71156	p-H <sub>2</sub> O 8 <sub>35</sub> –8 <sub>26</sub>
148.79410	p-H <sub>2</sub> O 5 <sub>42</sub> –6 <sub>15</sub>	156.19792	p-H <sub>2</sub> O 3 <sub>22</sub> –3 <sub>13</sub>
158.31551	p-H <sub>2</sub> O 3 <sub>31</sub> –4 <sub>04</sub>	159.48926	p-H <sub>2</sub> O 8 <sub>26</sub> –9 <sub>19</sub>
167.03912	p-H <sub>2</sub> O 6 <sub>24</sub> –6 <sub>15</sub>	169.74305	p-H <sub>2</sub> O 7 <sub>35</sub> –6 <sub>42</sub>
170.14342	p-H <sub>2</sub> O 6 <sub>33</sub> –6 <sub>24</sub>	174.61126	p-H <sub>2</sub> O 5 <sub>33</sub> –6 <sub>06</sub>
187.11543	p-H <sub>2</sub> O 4 <sub>13</sub> –4 <sub>04</sub>	208.08146	p-H <sub>2</sub> O 7 <sub>26</sub> –6 <sub>33</sub>
208.91861	p-H <sub>2</sub> O 9 <sub>46</sub> –10 <sub>19</sub>	222.95328	p-H <sub>2</sub> O 7 <sub>44</sub> –8 <sub>17</sub>
243.98004	p-H <sub>2</sub> O 2 <sub>20</sub> –2 <sub>11</sub>	248.25302	p-H <sub>2</sub> O 4 <sub>22</sub> –4 <sub>13</sub>
251.75737	p-H <sub>2</sub> O 8 <sub>53</sub> –7 <sub>62</sub>	255.68729	p-H <sub>2</sub> O 7 <sub>44</sub> –6 <sub>51</sub>
269.27908	p-H <sub>2</sub> O 1 <sub>11</sub> –0 <sub>00</sub>	303.46381	p-H <sub>2</sub> O 2 <sub>02</sub> –1 <sub>11</sub>
308.97175	p-H <sub>2</sub> O 5 <sub>24</sub> –4 <sub>31</sub>	327.23126	p-H <sub>2</sub> O 4 <sub>22</sub> –3 <sub>31</sub>
330.82984	p-H <sub>2</sub> O 9 <sub>28</sub> –8 <sub>35</sub>	398.65260	p-H <sub>2</sub> O 2 <sub>11</sub> –2 <sub>02</sub>
613.72660	p-H <sub>2</sub> O 6 <sub>24</sub> –7 <sub>17</sub>	631.57098	p-H <sub>2</sub> O 5 <sub>33</sub> –4 <sub>40</sub>
636.66801	p-H <sub>2</sub> O 6 <sub>42</sub> –5 <sub>51</sub>		

Several constraints are applied to the fitting process for PACS and SPIRE spectra. First, the line centroid is allowed to vary within  $\pm 2$  times the spectral resolution at the theoretical line centroid except for the [O I] line at 63.18  $\mu\text{m}$ . Because this line appears to have real velocity shifts in some sources, presumably due to wind motions, the line centroid is allowed to vary within  $\pm 3$  times the spectral resolution instead. Second, the linewidth is flexible in the fitting for SPIRE spectra, while the linewidth is fixed at the instrumental resolution for PACS spectra. The spectral resolution of PACS was insufficient to resolve most of the lines except for the [O I] line at 63.18  $\mu\text{m}$ . The linewidth of [O I] 63  $\mu\text{m}$  line is allowed to vary from –30% to 50% because this line may be broadened by the associated outflows. After comparing the fitting results with and without the linewidth fixed at the PACS instrumental resolution, we found that both strong lines and weak lines can be identified in the fixed-width setting with moderate S/N, while the flexible width setting produces better S/N on strong lines but might fit a narrower than reasonable feature at some wavelengths. The S/N of a strong emission line fitted with a

**Table 4**  
Line List for Single Gaussian Fitting: CO and  $^{13}\text{CO}$

CO		$^{13}\text{CO}$	
Wavelength ( $\mu\text{m}$ )	Line Name	Wavelength ( $\mu\text{m}$ )	Line Name
54.98622	CO $J = 48 \rightarrow 47$	209.48144	$^{13}\text{CO } J = 13 \rightarrow 12$
56.12190	CO $J = 47 \rightarrow 46$	226.90368	$^{13}\text{CO } J = 12 \rightarrow 11$
57.30773	CO $J = 46 \rightarrow 45$	247.49662	$^{13}\text{CO } J = 11 \rightarrow 10$
58.54705	CO $J = 45 \rightarrow 44$	272.21148	$^{13}\text{CO } J = 10 \rightarrow 9$
59.84349	CO $J = 44 \rightarrow 43$	302.42221	$^{13}\text{CO } J = 9 \rightarrow 8$
61.20106	CO $J = 43 \rightarrow 42$	340.18978	$^{13}\text{CO } J = 8 \rightarrow 7$
62.62410	CO $J = 42 \rightarrow 41$	388.75282	$^{13}\text{CO } J = 7 \rightarrow 6$
64.11741	CO $J = 41 \rightarrow 40$	453.50906	$^{13}\text{CO } J = 6 \rightarrow 5$
65.68791	CO $J = 40 \rightarrow 39$	544.17444	$^{13}\text{CO } J = 5 \rightarrow 4$
67.33814	CO $J = 39 \rightarrow 38$		
69.07614	CO $J = 38 \rightarrow 37$		
70.90902	CO $J = 37 \rightarrow 36$		
72.84469	CO $J = 36 \rightarrow 35$		
74.89194	CO $J = 35 \rightarrow 34$		
77.06064	CO $J = 34 \rightarrow 33$		
79.36181	CO $J = 33 \rightarrow 32$		
81.80787	CO $J = 32 \rightarrow 31$		
84.41284	CO $J = 31 \rightarrow 30$		
87.19261	CO $J = 30 \rightarrow 29$		
90.16527	CO $J = 29 \rightarrow 28$	173.63580	CO $J = 15 \rightarrow 14$
93.35147	CO $J = 28 \rightarrow 27$	186.00397	CO $J = 14 \rightarrow 13$
104.44758	CO $J = 25 \rightarrow 24$	200.27751	CO $J = 13 \rightarrow 12$
108.76555	CO $J = 24 \rightarrow 23$	216.93275	CO $J = 12 \rightarrow 11$
113.46045	CO $J = 23 \rightarrow 22$	236.61924	CO $J = 11 \rightarrow 10$
118.58370	CO $J = 22 \rightarrow 21$	260.24634	CO $J = 10 \rightarrow 9$
124.19648	CO $J = 21 \rightarrow 20$	289.12761	CO $J = 9 \rightarrow 8$
130.37221	CO $J = 20 \rightarrow 19$	325.23335	CO $J = 8 \rightarrow 7$
137.19978	CO $J = 19 \rightarrow 18$	371.65974	CO $J = 7 \rightarrow 6$
144.78783	CO $J = 18 \rightarrow 17$	433.56713	CO $J = 6 \rightarrow 5$
153.27056	CO $J = 17 \rightarrow 16$	520.24412	CO $J = 5 \rightarrow 4$
162.81572	CO $J = 16 \rightarrow 15$	650.26787	CO $J = 4 \rightarrow 3$

flexible width shows only a 6% increase compared to the S/N of the same line fitted with fixed-width setting. Therefore, for all lines other than [O I], we fix the FWHM of the line to the PACS spectral resolution. Users might be able to achieve a higher S/N, but we adopt the fixed width setting to avoid fake lines in this archive. For SPIRE, similar problems are not found due to a higher oversampling rate; thus we keep all line widths flexible within  $\pm 30\%$  of the SPIRE instrumental resolution. The instrumental resolution of PACS was obtained from personal communication with Dr. Helmut Feuchtgruber from MPE/Garching, and the instrumental resolution of SPIRE was obtained from the SPIRE data reduction guide released by *Herschel*.

#### 4.4. Blended Lines Fitting: Double Gaussian Fitting

Some emission lines are sufficiently blended that our default single Gaussian profile does not characterize the line shape. For known blended lines (listed in Table 7), we use a double Gaussian function to fit the blended profile. We only fit a double Gaussian model to two blended lines, while cases of more than two blended lines are fitted with a single Gaussian model for each component and labeled with blending condition (see next paragraph). The width of each component of blended lines are fixed to the instrumental spectral resolution. For blended lines, we require that both lines are in emission; if an absorption line is blended with an emission line, it cannot be fitted. When the fitting routine

reached the boundary and tried to fit a negative value to the line height, this value would be set to zero, resulting in a zero line flux in the report. Note that line fitting with a single Gaussian profile does allow negative flux values; this restriction on negative line flux values was only necessary for blended lines.

In the cases that a double Gaussian profile is not sufficient to distinguish two lines, the fitting process fits each line with a single Gaussian profile. If a detected single line can feasibly be identified with either of two lines in our linelist, depending on the physical properties or chemical composition of the source, we use a simple criterion to identify the possible blended regions as well as the likely dominant line. For any pair of lines with centroids located within one resolution element of each other, we classify the fit as a possible blended line, label the two options with Red and Blue indicating whether we attribute the blended line to the longer or shorter wavelength candidate. If a given line is not blended, we label it as x; if a line is blended with two other possible lines, the line is flagged with Red/Blue. Our recommended line identification is simply the line with the highest Einstein-A coefficient, as the level population dependence on physical conditions can be complicated. These blended lines are typically water lines with similar excitation requirements. These recommendations for line identification are recorded as 1 in the column Validity. These suggested identifications should be used with caution.

**Table 5**  
Line List for Single Gaussian Fitting: OH, HCO<sup>+</sup>, and CH<sup>+</sup>

OH		HCO <sup>+</sup> and CH <sup>+</sup>	
Wavelength ( $\mu\text{m}$ )	Line Name	Wavelength ( $\mu\text{m}$ )	Line Name
55.89231	OH $^2\Pi_{1/2,9/2}^+ - ^2\Pi_{1/2,7/2}^-$	210.28817	HCO <sup>+</sup> $J = 16 \rightarrow 15$
55.95141	OH $^2\Pi_{1/2,9/2}^- - ^2\Pi_{1/2,7/2}^+$	224.28136	HCO <sup>+</sup> $J = 15 \rightarrow 14$
65.13337	OH $^2\Pi_{3/2,9/2}^- - ^2\Pi_{3/2,7/2}^+$	240.27541	HCO <sup>+</sup> $J = 14 \rightarrow 13$
65.28048	OH $^2\Pi_{3/2,9/2}^+ - ^2\Pi_{3/2,7/2}^-$	258.73207	HCO <sup>+</sup> $J = 13 \rightarrow 12$
71.17262	OH $^2\Pi_{1/2,7/2}^- - ^2\Pi_{1/2,5/2}^+$	280.26712	HCO <sup>+</sup> $J = 12 \rightarrow 11$
71.21723	OH $^2\Pi_{1/2,7/2}^+ - ^2\Pi_{1/2,5/2}^-$	305.71952	HCO <sup>+</sup> $J = 11 \rightarrow 10$
79.11754	OH $^2\Pi_{1/2,1/2}^- - ^2\Pi_{3/2,3/2}^+$	336.26531	HCO <sup>+</sup> $J = 10 \rightarrow 9$
79.18106	OH $^2\Pi_{1/2,1/2}^+ - ^2\Pi_{3/2,3/2}^-$	373.60195	HCO <sup>+</sup> $J = 9 \rightarrow 8$
84.42237	OH $^2\Pi_{3/2,7/2}^+ - ^2\Pi_{3/2,5/2}^-$	420.27521	HCO <sup>+</sup> $J = 8 \rightarrow 7$
84.59877	OH $^2\Pi_{3/2,7/2}^- - ^2\Pi_{3/2,5/2}^+$	480.28810	HCO <sup>+</sup> $J = 7 \rightarrow 6$
115.15057	OH $^2\Pi_{1/2,5/2}^+ - ^2\Pi_{3/2,7/2}^-$	560.30913	HCO <sup>+</sup> $J = 6 \rightarrow 5$
115.38441	OH $^2\Pi_{1/2,5/2}^- - ^2\Pi_{3/2,7/2}^+$	60.24659	CH <sup>+</sup> $J = 6 \rightarrow 5$
119.23740	OH $^2\Pi_{3/2,5/2}^- - ^2\Pi_{3/2,3/2}^+$	72.13950	CH <sup>+</sup> $J = 5 \rightarrow 4$
119.44450	OH $^2\Pi_{3/2,5/2}^+ - ^2\Pi_{3/2,3/2}^-$	119.85466	CH <sup>+</sup> $J = 3 \rightarrow 2$
134.84152	OH $^2\Pi_{1/2,7/2}^- - ^2\Pi_{3/2,9/2}^+$	358.99894	CH <sup>+</sup> $J = 1 \rightarrow 0$
135.95981	OH $^2\Pi_{1/2,7/2}^+ - ^2\Pi_{3/2,9/2}^-$		
154.78349	OH $^2\Pi_{1/2,9/2}^+ - ^2\Pi_{3/2,11/2}^-$		
157.80984	OH $^2\Pi_{1/2,9/2}^- - ^2\Pi_{3/2,11/2}^+$		
163.12467	OH $^2\Pi_{1/2,3/2}^+ - ^2\Pi_{1/2,1/2}^-$		
163.40013	OH $^2\Pi_{1/2,3/2}^- - ^2\Pi_{1/2,1/2}^+$		

**Note.** The notation of OH transition follows the form of  $^2\Pi_{J_e,J_{\text{total}}}$ .  $J_e$  is the electron angular momentum quantum number, while  $J_{\text{total}}$  is the total angular momentum quantum number including electron and nuclear rotation. Please see more detail of the 163.12467  $\mu\text{m}$  OH line in Section 4.1.

We show two examples of double Gaussian fitting in Figure 7. In the top panel, we fit partially blended CO and [C I] emission lines. The bottom panel shows p-H<sub>2</sub>O and CO emission lines. In the first case, the fitting algorithm successfully resolved the blended lines, and both will be listed in the table of fitting results (see Section 4.6). In the second case, only the CO  $J = 18 \rightarrow 17$  line is detected, so the CO line will be reported as a detection and the p-H<sub>2</sub>O line as a non-detection.

In some spectral regions, there are three possible line candidates. We do not fit any triple Gaussian profiles due to the instability of such fits. Those lines are labeled in the same fashion. These regions will require individual fits with some a priori knowledge of the likely relative strengths of the three lines.

#### 4.5. Noise Estimation

The problem of noise estimation is two-fold. An accurate evaluation of the uncertainties of the fitted parameters needs a reliable uncertainty for each spectral data point. However, no uncertainties are provided for the SPIRE data, and those supplied for PACS are unrealistic. Therefore, the uncertainties of the spectral data points need to be estimated from the spectrum itself. After the baseline fitting, the fitting process proceeds in two ways, one for full SED scans and one for short scans (Section 2). We will describe the process first for the full SED scans (the majority of the sources) and then describe the changes needed for the sources with only short scans.

**Table 6**  
Line List for Single Gaussian Fitting: Atomic Fine-structure Lines

Wavelength ( $\mu\text{m}$ )	Line Name	Wavelength ( $\mu\text{m}$ )	Line Name
63.18367	[O I] $^3P_1 - ^3P_2$	121.911 $\pm$ 0.006 <sup>a</sup>	[N II] $^3P_2 - ^3P_1$
145.48056	[O I] $^3P_0 - ^3P_1$	157.69228	[C II] $^2P_{3/2} - ^2P_{1/2}$
205.170 $\pm$ 0.004 <sup>a</sup>	[N II] $^3P_1 - ^3P_0$	230.34913	[C I] $^3P_2 - ^3P_0$
370.42438	[C I] $^3P_2 - ^3P_1$	609.15069	[C I] $^3P_1 - ^3P_0$

**Note.**

<sup>a</sup> The mean values and the standard deviation of the mean of line centeroids are measured from the corresponding fitted lines with  $S/N > 10$ . The initial guesses were 121.9, and 205.178  $\mu\text{m}$ .

For sources with full SED scans, we feed the fitting routine with the spectra three times, two to precisely measure the uncertainties from the fluctuations of the baseline (hereafter baseline noise) and one to apply the baseline noise as the uncertainties of the spectral data points to get an accurate evaluation of the uncertainties of fitted line parameters (Figure 8). The baseline noise is fed into the final fitting process to get the final fitted parameters with uncertainties. Each time the lines are fitted, the S/N of the line flux ( $F_l$ ) is calculated by taking the line strength divided by the standard deviation of the modified baseline (the baseline with continuum removed) times the square root of the oversampling rate and the FWHM of the line and 1.064 for a Gaussian profile

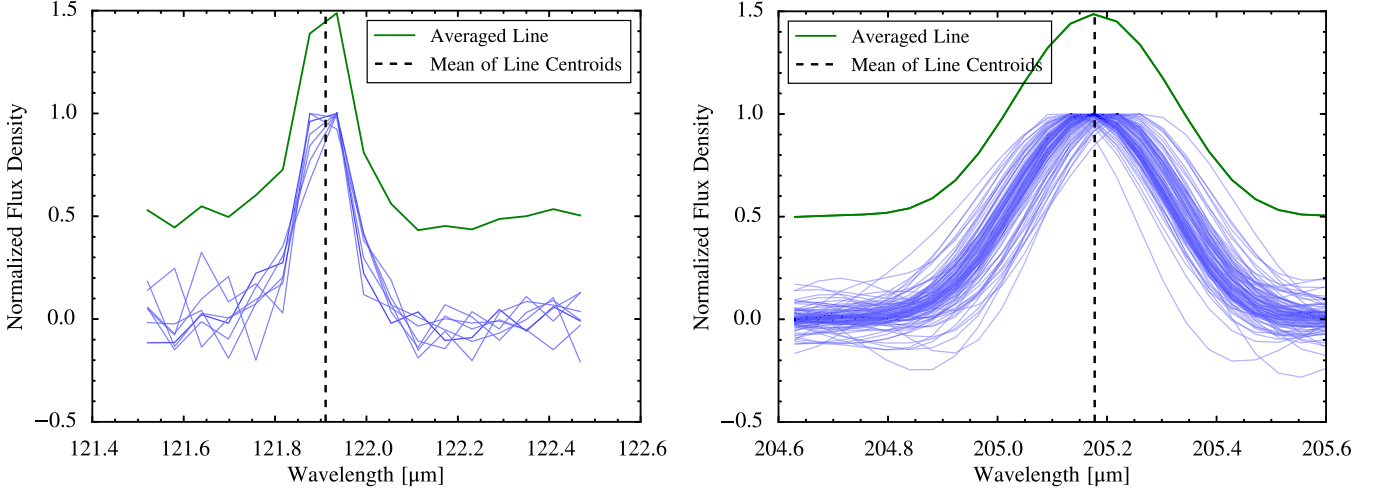


**Figure 6.** The line profiles of [N II] 122  $\mu\text{m}$  and [N II] 205  $\mu\text{m}$  lines identified in this archive with S/N greater than 10. The individual line profiles are shown in blue, while the averaged line profile is shown in green. The line centroids of the averaged line profiles are reported in Table 6.

**Table 7**  
Blended Lines Fit with Double Gaussian Profile

Wavelength ( $\mu\text{m}$ )		Line Names	
55.85970	55.89231	p-H <sub>2</sub> O 6 <sub>51</sub> -7 <sub>26</sub>	OH $^2\Pi_{1/2,9/2}^+ - ^2\Pi_{1/2,7/2}^-$
55.95141	55.98480	OH $^2\Pi_{1/2,9/2}^- - ^2\Pi_{1/2,7/2}^+$	p-H <sub>2</sub> O 7 <sub>71</sub> -7 <sub>62</sub>
56.77240	56.81777	p-H <sub>2</sub> O 9 <sub>19</sub> -8 <sub>08</sub>	o-H <sub>2</sub> O 9 <sub>09</sub> -8 <sub>18</sub>
65.13337	65.16779	OH $^2\Pi_{3/2,9/2}^- - ^2\Pi_{3/2,7/2}^+$	o-H <sub>2</sub> O 6 <sub>25</sub> -5 <sub>14</sub>
71.17262	71.21723	OH $^2\Pi_{1/2,7/2}^- - ^2\Pi_{1/2,5/2}^+$	OH $^2\Pi_{1/2,7/2}^+ - ^2\Pi_{1/2,5/2}^-$
75.81532	75.83188	p-H <sub>2</sub> O 7 <sub>53</sub> -7 <sub>44</sub>	o-H <sub>2</sub> O 6 <sub>52</sub> -6 <sub>43</sub>
79.11754	79.18106	OH $^2\Pi_{1/2,1/2}^- - ^2\Pi_{3/2,3/2}^+$	OH $^2\Pi_{1/2,1/2}^+ - ^2\Pi_{3/2,3/2}^-$
84.41284	84.42237	CO $J = 31 \rightarrow 30$	OH $^2\Pi_{3/2,7/2}^- - ^2\Pi_{3/2,5/2}^+$
113.46045	113.54021	CO $J = 23 \rightarrow 22$	o-H <sub>2</sub> O 4 <sub>14</sub> -3 <sub>03</sub>
118.40826	118.58370	p-H <sub>2</sub> O 9 <sub>37</sub> -8 <sub>44</sub>	CO $J = 22 \rightarrow 21$
130.32199	130.37221	CO $J = 20 \rightarrow 19$	p-H <sub>2</sub> O 7 <sub>53</sub> -8 <sub>26</sub>
134.84152	134.93863	OH $^2\Pi_{1/2,7/2}^- - ^2\Pi_{3/2,9/2}^+$	o-H <sub>2</sub> O 5 <sub>14</sub> -5 <sub>05</sub>
156.19792	156.26908	p-H <sub>2</sub> O 3 <sub>22</sub> -3 <sub>13</sub>	o-H <sub>2</sub> O 5 <sub>23</sub> -4 <sub>32</sub>
144.52144	144.78783	p-H <sub>2</sub> O 4 <sub>13</sub> -3 <sub>22</sub>	CO $J = 18 \rightarrow 17$
166.81885	167.03912	o-H <sub>2</sub> O 7 <sub>34</sub> -7 <sub>25</sub>	p-H <sub>2</sub> O 6 <sub>24</sub> -6 <sub>15</sub>
174.61126	174.63028	p-H <sub>2</sub> O 5 <sub>33</sub> -6 <sub>06</sub>	o-H <sub>2</sub> O 3 <sub>03</sub> -2 <sub>12</sub>
259.98875	260.24634	o-H <sub>2</sub> O 3 <sub>12</sub> -2 <sub>21</sub>	CO $J = 10 \rightarrow 9$
272.21148	273.19988	<sup>13</sup> CO $J = 10 \rightarrow 9$	o-H <sub>2</sub> O 3 <sub>12</sub> -3 <sub>03</sub>
302.42221	303.46381	<sup>13</sup> CO $J = 9 \rightarrow 8$	p-H <sub>2</sub> O 2 <sub>02</sub> -1 <sub>11</sub>
370.42438	371.65974	[C I] <sup>3</sup> P <sub>2</sub> - <sup>3</sup> P <sub>1</sub>	CO $J = 7 \rightarrow 6$
609.15069	613.72660	[C I] <sup>3</sup> P <sub>1</sub> - <sup>3</sup> P <sub>0</sub>	p-H <sub>2</sub> O 6 <sub>24</sub> -7 <sub>17</sub>

(Equation (1)).

$$\text{S/N} = \frac{F_1}{1.064 \sigma_{\text{baseline}} \sqrt{\text{oversampling}} \times \text{FWHM}}. \quad (1)$$

During the first pass through the data (left panel of Figure 8), the routine attempts to identify and remove all lines in the line list and calculates a first estimate of the S/N using a restricted baseline range ( $\pm 10$  spectral resolution elements around the line centroid). This modification is designed to include enough

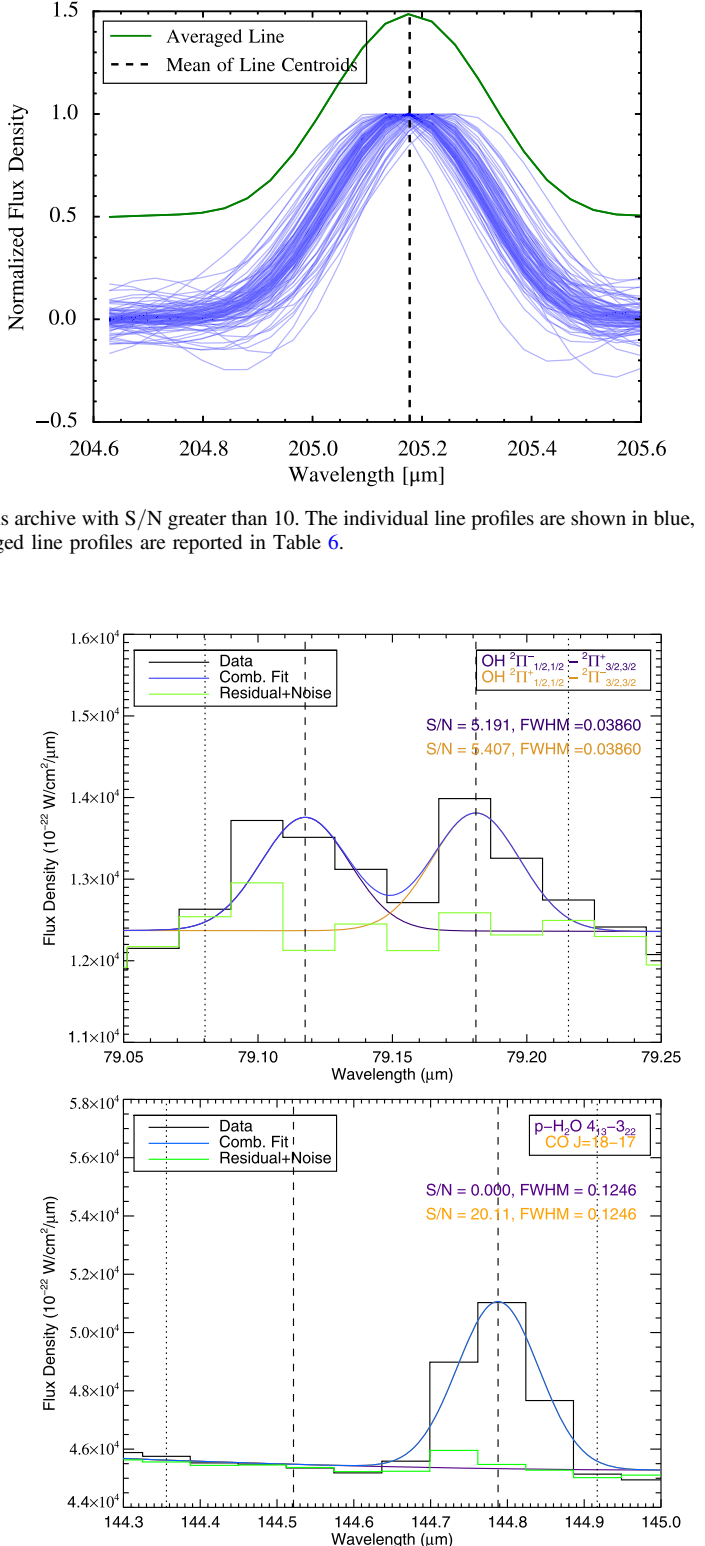


**Figure 7.** Examples of double-Gaussian fitting. Top: for the blended OH  $^2\Pi_{1/2,1/2}^- - ^2\Pi_{3/2,3/2}^+$  line and the OH  $^2\Pi_{1/2,1/2}^+ - ^2\Pi_{3/2,3/2}^-$  line, for L1157, using fixed line centroids and FWHM constraints. The lines plotted are data (black), combined fit (blue), OH  $^2\Pi_{1/2,1/2}^- - ^2\Pi_{3/2,3/2}^+$  fit (purple), OH  $^2\Pi_{1/2,1/2}^+ - ^2\Pi_{3/2,3/2}^-$  fit (yellow), and residual (green) (See Section 4.5). The S/N of the two OH lines are 6.38 and 6.65, respectively. Both lines are considered as detections. Bottom: an example of a double fit in which only a single component was detected. We show the blended p-H<sub>2</sub>O 4<sub>13</sub>-3<sub>22</sub> and CO  $J = 18 \rightarrow 17$  lines, for BHR71, using fixed line centroids and FWHM constraints. The color code is the same as the top figure. The S/N of the CO line is 25 and is significant; the p-H<sub>2</sub>O line is not detected.

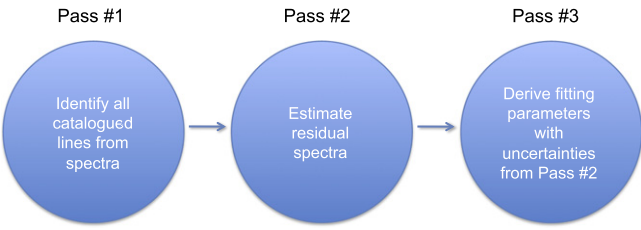


**Figure 8.** Summary of the three passes to fit spectral lines from an input 1D spectrum.

wavelength channels in the baseline while avoiding contamination from nearby strong lines. It is a rough estimation, which will be refined if the full noise estimation process can be performed.

In the first fitting process, every line is fitted without any prior knowledge of other lines. This first estimate occasionally yields anomalous uncertainties for blended lines or lines with other lines nearby, as the residual after subtracting the fitted line is not only the noise but also other, not-yet-fitted, emission lines. Thus in the second pass of the data, we subtract all lines identified with  $S/N > 2$  ( $S/N$  calculated from the noise biased by not-yet-fitted lines) from the whole spectrum. Then we use a top-hat smoothing function to approximate the continuum shape. We then subtract the continuum to produce a residual spectrum without any contamination, which is the main goal of the second pass (middle panel of Figure 8).

With the improved estimation of the uncertainties of the data points in hand, a third line fitting is executed (right panel of Figure 8), producing reliable uncertainties of fitted parameters. The extra two steps in the line fitting routine increase the  $S/N$  by 23% (38% for strong lines). The smoothing function and continuum subtraction are also applied during the third fitting. The  $S/N$ s are calculated from the residual spectra from the third fitting. The fitting results produced from the third fitting, as well as the continuum, flat, and residual spectra, are those reported in the archive (examples in Figure 9). The continuum spectrum is the best product for modeling dust continuum emission. The flat spectrum provides an overview of the line emission, and the residual spectrum can be examined for unidentified lines or anomalies in the line fitting process.

For the short scan sources, the continuum coverage is insufficient to derive a complete continuum spectrum; consequently the estimate of the baseline noise is less precise and nearby lines could be adding to the noise. The second fitting process for those data uses the noise estimated from the first pass as the uncertainties in the fitting process to derive the fitted parameters with uncertainties. There is no third pass for those sources. The fits with all three fitting processes are labeled as “Global,” while the ones with only two fitting processes are labeled as “Local” in the “full\_source\_list.txt” file (see Section 4.6).

By feeding in realistic uncertainties of the spectra, we can calculate reasonable uncertainties in the fitted parameters of the line. In Figure 10, we show the relation between the two different uncertainties, the uncertainty from the baseline and the uncertainty in the fitted line flux. Most uncertainties calculated by both methods correlate well with each other, for both PACS and SPIRE data, verifying that the uncertainties are correctly processed in the fitting routine.

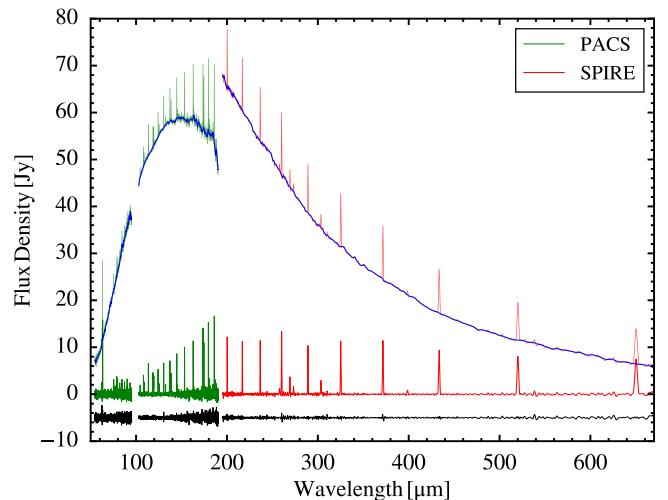


**Figure 9.** The spectrum of L1157 with flat spectrum (green/red for PACS/SPIRE, respectively), continuum (blue), and residual (black, offset by  $-5\text{ Jy}$ ) overplotted. The continuum is the result of the smoothing function applied to the line-subtracted spectrum. The flat spectrum is produced by removing the continuum from the original spectrum. The residual spectrum is resulted from subtracting the continuum and fitted lines from the original spectrum. The comparison of the continuum and the flat spectrum at the edge of the PACS band shows that the fitting algorithm works well even in the region with severe instrumental effects. The offset between PACS and SPIRE spectra is discussed in Section 3.2.

While the uncertainties determined by each method (baseline fitting and line fitting) are similar (marked by a “line of equality”), there are some interesting features. In both figures, the points spread over about two orders of magnitude, partly reflecting the higher noise in some modules (see Figure 3 for example) and partly due to the changing FWHM in wavelength space, especially for SPIRE. The distributions of the uncertainties measured in different modules of both PACS and SPIRE show a Gaussian-like distribution with a tail toward higher uncertainty. For PACS, the uncertainty distribution of each module centers at different values with B2A highest, B2B in middle, and R1 lowest. The two R1 modules have a similar distribution, although the data are processed separately. For SPIRE, the SLW module has an uncertainty distribution peaking at a lower value compared to SSW. Finally, there is a spread of fits that lie above the line of equality reflecting the fact the the assumed line profile is not always a good fit to the data.

#### 4.6. Reporting of Line-fitting Results

The results from the fitting routine are written in the folder called `advanced_products`, part of the archive structure described in Section 5. The results include information on the fitted line parameters, as well as the flat spectrum, pure continuum spectrum, and residual spectrum (Figure 9). The offset between PACS and SPIRE spectra is discussed in Section 3.2. Guidelines for properly interpreting the report are discussed below.

These text files are named `object_reduction_trim-lines.txt`, and they contain all of the information necessary to reconstruct the line fits. These ASCII table contains either 18 or 19 columns (for the 1D spectrum or the spectrum of a single spaxel, respectively).

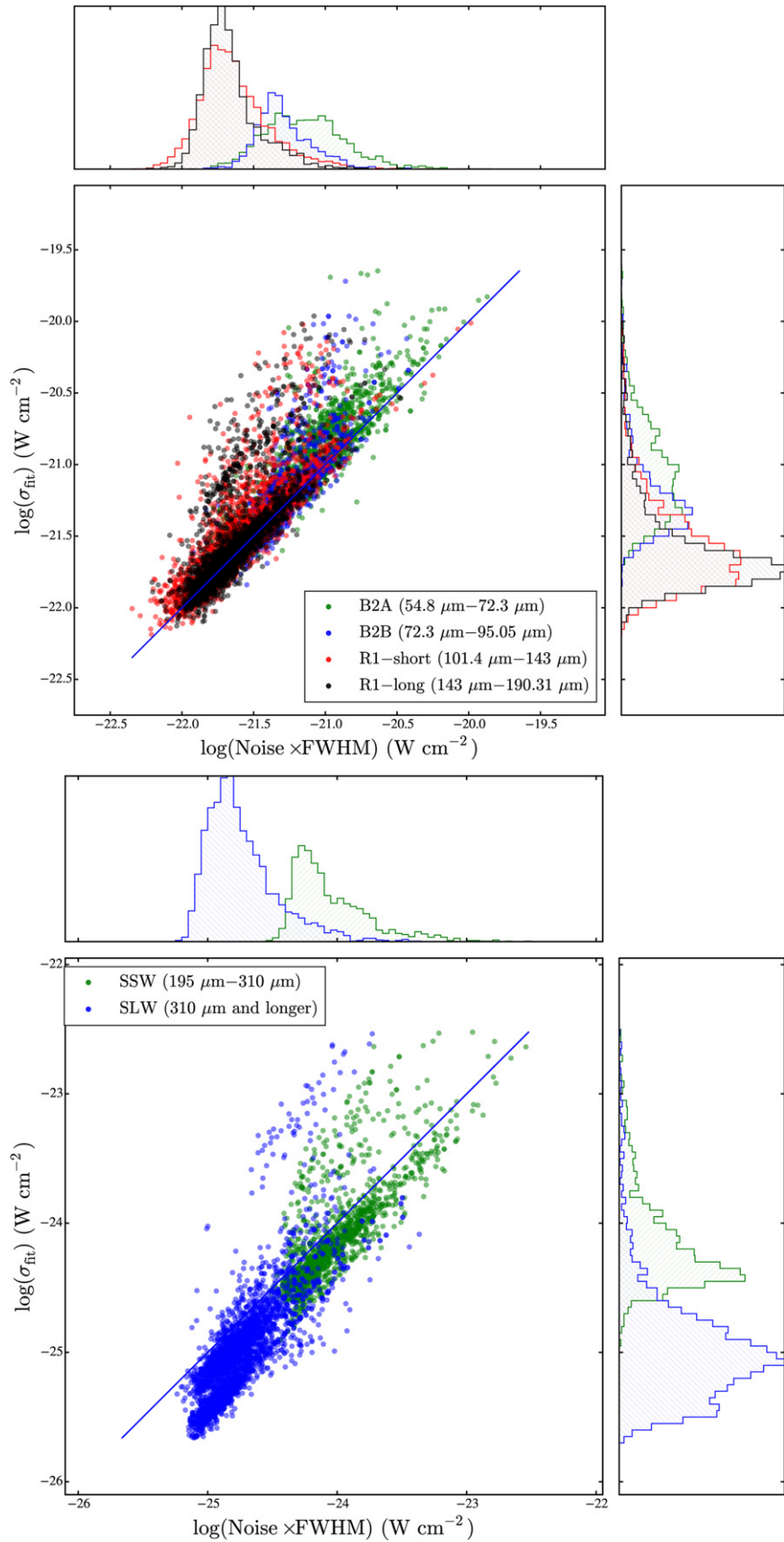


**Figure 10.** The correlations of the uncertainties measured from the baseline and the uncertainties of the fitted parameters (Top: PACS, Bottom: SPIRE). Detections with different modules are presented in different colors (see legends). The blue line indicates the equality of two quantities with zero offset.

**Table 8**  
A Portion of the 1D Spectrum Fitting Results for BHR71

Line	LabWL (um)	ObsWL (um)	Sig_Cen (um)	Str (W/cm2)	Sig_str (W/cm2)	
CO48-47	54.98621750	54.98154779	0.03082777749	-2.277802385e-21	2.967605715e-21	
p-H204_31-3_22	56.32640076	56.30309023	0.007689705798	8.970946845e-21	2.958435088e-21	
CO46-45	57.30772781	57.30463621	0.2850716473	-2.699435981e-22	3.260885618e-21	
o-H206_61-6_52	63.91602325	63.93649292	-999.0000000	2.197260987e-21	2.763702731e-21	
o-H207_61-7_52	63.95696259	63.93729134	0.02943608129	2.198141514e-21	2.764042837e-21	
p-H209_37-8_44	118.4082565	118.4959793	-999.0000000	3.497948853e-20	1.314679686e-20	
CO22-21	118.5837021	118.5876394	0.003691032704	7.394416427e-20	3.865617628e-21	
p-H208_35-8_26	148.7115631	148.7528381	-999.0000000	-3.672127599e-21	1.629373707e-21	
CO4-3	650.2678833	650.2828864	0.01499258376	4.128831785e-20	6.530348726e-22	
CI3P2-3P1	370.4243774	370.4243774	-998.0000000	0.000000000	-998.0000000	
FWHM (um)	Sig_FWHM (um)	Base (W/cm2/um)	Noise (W/cm2/um)	S/N	E_u (K)	
0.03897858372	-998.0000000	5.860891006e-18	8.720767999e-20	0.6297869004	6457.230000	
0.03906316840	-998.0000000	6.295500447e-18	8.226700068e-20	2.623635637	552.3000000	
0.03912018226	-998.0000000	6.354233016e-18	1.049475567e-19	0.06179569179	5939.210000	
0.03936703190	-998.0000000	7.381455348e-18	6.509757235e-20	0.8058283595	1503.600000	
0.03936783131	-998.0000000	7.381706869e-18	7.165146509e-20	0.7323985066	1749.900000	
0.1169993003	-998.0000000	6.777696602e-18	9.334557437e-20	3.010196356	1749.900000	
0.1170676737	-998.0000000	6.772795551e-18	3.430364591e-20	17.30553393	1397.380000	
0.1251977122	-998.0000000	4.240183287e-18	1.615138300e-20	1.706750436	1511.000000	
2.951818452	0.03529221031	1.568093311e-20	3.629903522e-22	36.21602920	55.32000000	
0.9943682530	-998.0000000	2.116988821e-19	1.348351580e-21	0.000000000	62.46200000	
A (s-1)	g	RA (deg)	Dec (deg)	Pixel_No.	Blend	Validity
0.006556000000	97	180.3982553	-65.14761521	c	x	1
1.452000000	9	180.3982553	-65.14761521	c	x	1
0.006091000000	93	180.3982553	-65.14761521	c	x	1
0.35330000000	39	180.3982553	-65.14761521	c	Red	0
0.58280000000	45	180.3982553	-65.14761521	c	Red/Blue	0
0.01724000000	19	180.3982553	-65.14761521	c	Red	0
0.001006000000	45	180.3982553	-65.14761521	c	Red/Blue	1
0.12350000000	17	180.3982553	-65.14761521	c	Red	0
6.126000000e-06	9	180.4010925	-65.14799500	c	x	1
2.650000000e-07	5	180.4010925	-65.14799500	c	DoubleGaussian	1

**Note.** The tables in the ASCII files have the same columns and style except that the rows are chopped into three parts here for better display. Also this table has selected lines from different parts of the original results to demonstrate different flags, etc. As mentioned in Section 4.6, any column with -999 indicates a fitting result that is not well-constrained. Therefore, the Validity flag is set to be 0. The Pixel\_No. Column lists “c” for the 1D spectrum measurements, and the specific pixel number/name for cube measurements.

(This table is available in its entirety in machine-readable form.)

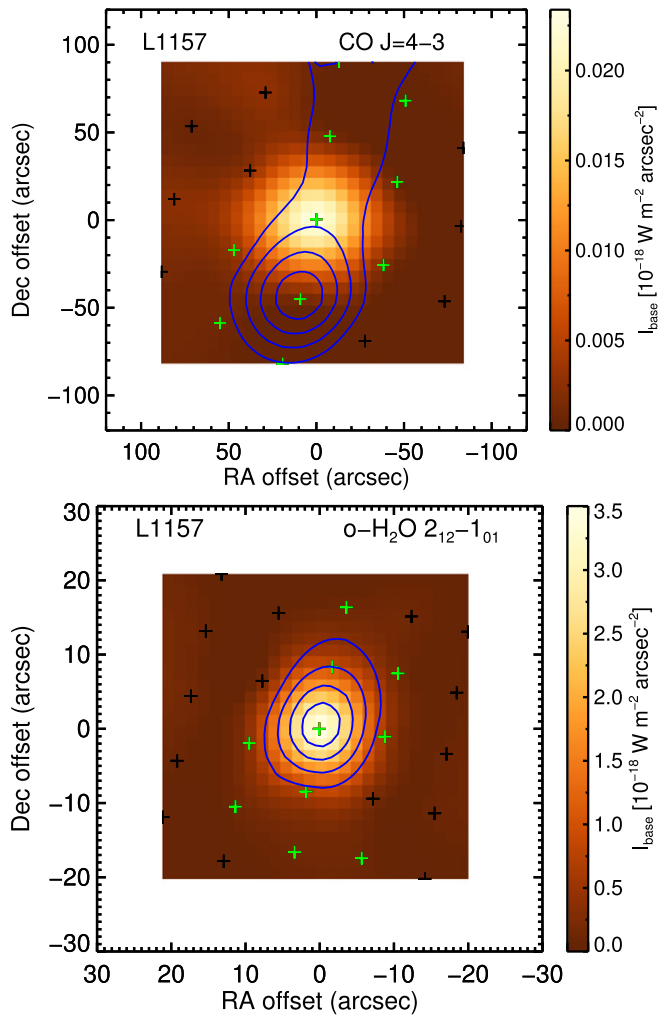


**Figure 11.** An example of 2D contour maps of L1157 CO  $J = 4 \rightarrow 3$  and o-H<sub>2</sub>O 2<sub>12</sub>-1<sub>01</sub> line emission (blue contours) with local continuum (filled background) observed in SPIRE and PACS respectively. The green crosses indicate the spaxels that have detections.

There are some caveats that should be considered before applying the results. Note that every line checked for a fit is listed, so many will be non-detections. Choosing a suitable minimum S/N would be necessary to select likely detections. Then further quality control checks should be applied. First, the “Validity” column should be 1 for each unique plausible line detection. If an uncertainty column indicates -999, the fit was unsuccessful and the fitted parameter and its uncertainty value should not be used; all lines flagged with -999 in any column should be discarded. The -999 flag is applied to the columns of Sig\_Cen\_WL(um) and Sig\_FWHM(um) if the quality of the fit is poor. This flag indicates that the line profile reached the local  $\chi^2$  minimum by moving to the edge of the allowed parameter space, stopping only due to imposed fitting constraints. In this case, the fitting routine is probably not identifying the input emission line. We do not recommend using any line flagged as 0 in Validity or -999 in other columns, except for the [O I] 63  $\mu$ m line, which can be wider than expected. We strongly encourage users to check the fitting plots of [O I] 63  $\mu$ m lines before applying the results.

If an uncertainty column is flagged as -998, the fitted parameters can be used, but the uncertainties will need to be extrapolated from other nearby line fits. The -998 flag appears only in the uncertainty columns Sig\_FWHM(um), Sig\_Cen\_WL(um) and Sig\_Str(W/cm<sup>2</sup>), and only if the line width is fixed to a particular value (the instrumental resolution at that wavelength). In this case uncertainties cannot be generated, but the fitted parameters are considered reliable. We fix most line widths in PACS line fits (an exception is [O I] 63  $\mu$ m, which has been observed to be broader than the instrumental line width), but only fix the width for cases of double-Gaussian fitting in SPIRE line fits. In these cases of fixed line width, we cannot calculate uncertainties for the line width. If an uncertainty is needed, we recommend using values for a nearby line if available. A portion of the fitting results table is shown in Table 8; the full table is available in the online manuscript.

A summary of sources and how they were processed can be found at “full\_source\_list\_refine.txt.” It lists the names of the processed sources in order and the status of access to different reductions. Additional information can be found in the file “full\_source\_list.txt,” which includes the information about the noise re-estimation (see Section 4.5).

In total, we performed line fitting on 67 and 33 objects in the PACS and SPIRE bands, respectively. 2D PACS datacubes consist of four modules of 25 spaxels each, and SPIRE datacubes consist of two modules of 33 and 19 spaxels, for SSW and SLW respectively. Including all spaxels in the 2D datacube, totaling 264590 PACS and 60330 SPIRE line fitting processes, we found 10474 and 4985 detections without any anomaly in PACS and SPIRE fits, compared to 254116 and 55345 non-detections, including anomalies (fits with S/N > 3 but a flag for poor fitting quality applied). Any line fit in which an unphysical broad component was fitted, the line centroid diverged and reached our pre-defined boundary, or the fitted line was blended with another line with lower Einstein-A value, was determined to be an anomaly. There were a total of 322 and 1334 anomalies in the PACS and SPIRE fits. On average, we found 156 and 151 lines per object in PACS and SPIRE bands, including all spatial positions. The fitting results of all PACS and SPIRE sources are also stored in four ASCII files for 1D and 2D spectra (“CDF\_archive\_pacs[spire]\_1d[cube]\_lines.txt”).

#### 4.7. Contour Plots

To further visualize the fitting results, we produce contour plots of each line (line contours) overplotted on the local continuum at the wavelength of the line centroid (e.g., Figure 11). We plot contours only for maps with detections in *more* than 2 spaxels; however, plots with continuum emission are provided for maps with fewer detections. The contours are the minimum curvature surface interpolated from lines with S/N greater than 3. The adjacent contours are in steps of 20% of the peak, while the lowest 20% contour is not shown. The crosses (white) in each figure indicate the physical position of each spaxel and the center cross indicates the pointing position. The crosses marked in green indicate spaxels with significant line detections; users can judge the reliability of detailed structure in an individual contour plot based on the number and location of spaxels with detections.

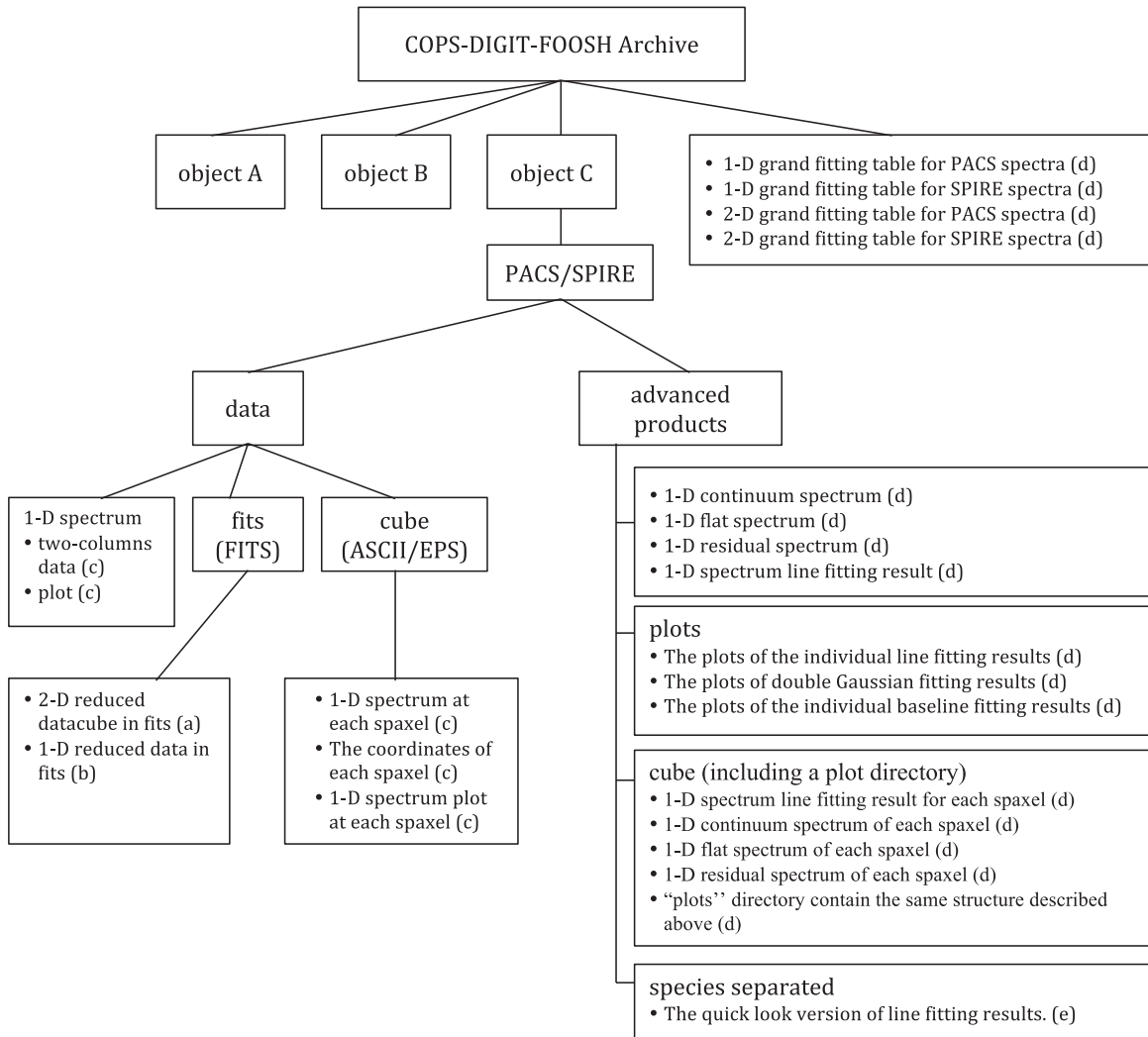


**Figure 12.** The hierarchy structure of the archival file system. Files are organized primarily by the targets, and every target directory has the same substructure. The PACS and SPIRE high-level data and fitting results are stored in separate directories with the same structure. The letters refer to the sub-headings describing the products in Section 5.2.

## 5. ARCHIVE STRUCTURE AND FILE FORMAT

The archive can be accessed through the HSA under User Provided Data Products<sup>12</sup> or as a downloadable archive file.<sup>13</sup> The file and directory trees contained in the archive are indicated in Figure 12. We provide the high-level data from the optimized pipeline and the products of line fitting results. The following section describes the file structure and how to interpret the individual formats.

### 5.1. File Structure

The schematic view of the file structure is shown in Figure 12. If there is no PACS or SPIRE observation available for a target, then the corresponding directory is not present. The detailed description of each product is described below. The products are identified in Figure 12 with the same letter (a through e) used to identify the following sections.

### 5.2. File Format

<sup>12</sup> <http://www.cosmos.esa.int/web/herschel/user-provided-data-products>

<sup>13</sup> [ftp://hsa.esac.esa.int/LEGACY\\_PRODUCTS/UPDP/DIGIT/](ftp://hsa.esac.esa.int/LEGACY_PRODUCTS/UPDP/DIGIT/)

#### (a) 2D reduced datacubes (FITS)

##### (1) PACS

We generate three datacubes for PACS in FITS format: Source–Nod A; Source–Nod B; Average (Source–(Nod A+Nod B)/2). These can be read as dataplanes for each spaxel, with appropriate R.A./decl., and flux versus wavelength. They are generated with wavelength grid oversample = 2 and upsample = 1 by default. These cubes include all corrections (in particular jitter correction).

Filename:

```

OBSID_1342xxxxxx_Targetname_blue/
red_rebinnedcubesnoda_os#sf#.fits
OBSID_1342xxxxxx_Targetname_blue/
red_rebinnedcubesnodb_os#sf#.fits
OBSID_1342xxxxxx_Targetname_blue/
red_finalcubes_os#sf#.fits
  
```

We also generate these same three cubes *without* the pointing offset correction, with the addition of “\_nojitter.fits” to the filename. We include the offset-corrected product only if the correction was successful. We include the non-offset corrected

version for *all* sources. If a jitter-corrected version is supplied, it means that we recommend using it.

## (2) SPIRE

We generate one datacube for SPIRE in FITS format. These can be read as dataplanes for each spaxel, with appropriate R.A./decl., and flux versus wavelength. Note that both SLW and SSW modules are included in a single FITS file. These cubes include all corrections.

Filename:

```
1342xxxxxx_spectrum_extended_H-
R_aNB_15.fits
```

There is no offset-corrected product being generated for SPIRE data.

## (b) 1D reduced spectra (FITS)

### (1) PACS

We generate FITS files for three cases listed below, each with and without jitter correction; all six resulting files have the point source point-spread function (PSF) correction applied. We also provide files in ASCII and EPS formats (see next section).

Filename:

```
OBSID_1342xxxxxx_Targetname_blue/
red_centralSpaxel_PointSourceCorrec-
ted_Corrected3x3NO_slice00_os#sf#.
fits
```

This is the simplest product, which is just the spectrum of the central spaxel with only the PSF correction applied. The “slice” is only non-zero for multiple rangescan or linescan observations, representing different wavelength settings within the original OBSID.

Filename:

```
OBSID_1342xxxxxx_Targetname_blue/
red_centralSpaxel_PointSourceCorrec-
ted_Corrected3x3YES_slice00_os#sf#.
fits
```

This is the same as the above product but with the jitter/pointing correction for the loss of light between pixels included in addition to the PSF correction. That is, we start with the central spaxel, and apply both the PSF and pointing/jitter correction.

We also generate the straight sum of the  $3 \times 3$  spaxels, including PSF and pointing/jitter corrections:

Filename:

```
OBSID_1342xxxxxx_Targetname_blue/
red_central9Spaxels_ PointSourceCor-
rected_slice00_os#sf#.fits
```

A summation of the central 9 spaxels (the “ $3 \times 3$ ” case) with PSF correction applied. So in summary, all three files have the point source (PSF) correction applied. The “ $3 \times 3$ NO” is just this raw product. The “ $3 \times 3$ YES” is the flux of the central spaxel after correcting for the PSF and the pointing/jitter. The “central9Spaxels” is the sum of the flux in the central  $3 \times 3$  spaxels, still including the PSF/pointing jitter corrections. We also output a version of these files without the pointing/jitter corrections. The filename is similar to the previous version, but with “\_nojitter.fits” appended; “nojitter” refers to no jitter corrections applied.

We compare the three products for the case of

L1157 in Figure 13. The blue spectrum shows the centralSpaxel product without the absolute flux calibration of the  $3 \times 3$  aperture extraction; the red spectrum is the straight sum of the central  $3 \times 3$  spaxels, and the black spectrum is the best product, combining the S/N of the central spaxel with the absolute flux calibration of the  $3 \times 3$  aperture extraction.

## (2) SPIRE

We generate one FITS file containing the SPIRE 1D spectrum for each target. The spectra are processed by the pipeline setting described in Section 3.2 including “SemiExtendedSourceCorrector” routine.

Filename:

```
Targetname_spire_corrected.fits
```

In this FITS file, all of the dataplanes are ordered as in the 2D datacube. But only dataplanes 5 and 8 containing the central spaxel in SLW and SSW are the ones with corrected values. The lines are fitted from these spectra as well.

## (c) 1D reduced spectra (two-columns ASCII/EPS)

For both the 1D reduced spectra and 2D datacubes, we extract the information (wavelength and flux) from the FITS files and report them in two-column ASCII format with plots of the corresponding spectrum for each spaxel or source. The same plotting method is applied to both 1D spectra and spaxels within the datacubes. In PACS, we combine all of the modules (B2A, B2B and R1, see Section 2) together in ASCII files and plots. In addition, because the pointing coordinate of each spaxel varied slightly with wavelength, the files ending with “coord” contain the coordinates (R.A./decl.) of each spaxel at each wavelength point. The coordinates reported in the 1D spectra fitting results table are derived from the mean values of the coordinates across all wavelengths. The standard deviations of the coordinates across all wavelengths range from from  $0.^{\circ}0073$  to  $0.^{\circ}354$  for R.A., and  $0.^{\circ}0233$  to  $0.^{\circ}4386$  for decl. The mean values of the standard deviation are  $0.^{\circ}129$  and  $0.^{\circ}0675$  in R.A. and decl. respectively. But different modules are reported separately for SPIRE due to their different spaxel configurations. We recommend using the coordinates from the files we provided instead of reading in from the header of the FITS files.

Filename:

(1D)

```
Targetname_reduction_trim.txt
```

```
Targetname_reduction_trim.eps
```

(2D)

```
Targetname_pacs_pixel##_os#sf#.txt
```

```
Targetname_pacs_pixel##_os#sf#_-
coord.txt
```

```
Targetname_pacs_pixel##_os#sf#.eps
```

```
Targetname_pixelname.txt
```

```
Targetname_pixelname.eps
```

These ASCII files (and the corresponding EPS plots) are trimmed consistently at specific wavelengths. Here we describe trimming details for PACS and SPIRE separately.

### (1) PACS

For the shortest wavelength module (B2A), we remove all wavelengths short of  $54.80 \mu\text{m}$ , and long

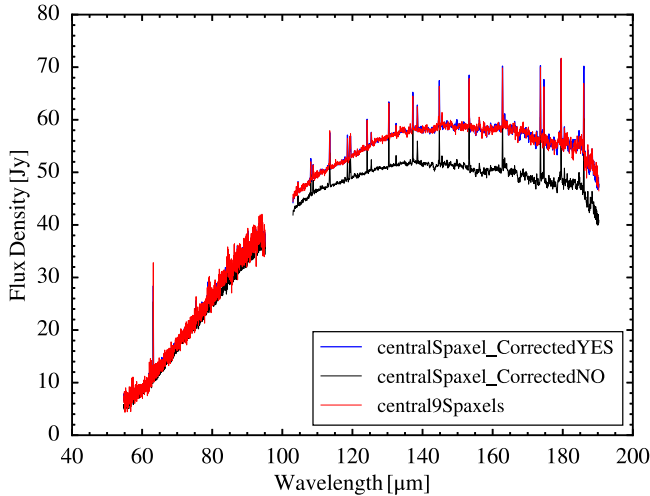


**Figure 13.** Plot of our three PACS pipeline products, for protostar L1157. The blue spectrum shows the central spaxel product, with best S/N without accounting for source extent. The red spectrum is the sum of the central 9 spaxels in the PACS array; this likely includes all of the source flux, but also added noise from low S/N spaxels. The black spectrum is the best compromise product, flux calibrated to the red spectrum that has most of the source flux, but with S/N consistent with the blue spectrum. Note that lines are stronger in black than red with only modest increase of noise, therefore higher S/N.

of  $72.3\text{ }\mu\text{m}$ . For the next shortest (B2B), we trim all wavelengths short of  $72.3\text{ }\mu\text{m}$  and long of  $95.05\text{ }\mu\text{m}$ . For the third (R1;  $100\text{--}145\text{ }\mu\text{m}$ ), we remove all wavelengths short of  $101.4\text{ }\mu\text{m}$  and long of  $143.0\text{ }\mu\text{m}$ . For the fourth (R1;  $145\text{--}210\text{ }\mu\text{m}$ ), we trim all wavelengths short of  $190.31\text{ }\mu\text{m}$  and long of  $143.0\text{ }\mu\text{m}$ .

## (2) SPIRE

For the shorter wavelength module (SSW), we remove all wavelengths short of  $195\text{ }\mu\text{m}$  and long of  $310\text{ }\mu\text{m}$ . For the longer wavelength module (SLW), we remove all wavelengths short of  $310\text{ }\mu\text{m}$ .

We find this method gives the best overall continuum fit between modules, with the highest S/N and consistent continuum in the overlap regions, stitched into a single 1D spectrum. Figure 14 shows the original spectra from all modules, and the shaded regions indicate the part preserved after the trimming. The regions where the continuum behaves abnormally and/or the noise increases significantly are excluded via the trimming process. Note that the original, untrimmed spectra are still present in our archive. The FITS files previously described do not use these trim points and present the full spectra from all modules. An example of the final trimmed spectra of the protostar L1157 (PACS and SPIRE) is shown in Figure 15, with each module highlighted by color.

## (d) Line fitting results

The line fitting results are reported in text and figures format. The ASCII files provide the tables of the fitting results so that users can read them in with any language they prefer. The figures visualize the fitting results with the original data, fitted line(s), and residual. The users can visually check the fitting results with the figures easily.

Filename:

(PACS)

Targetname\_reduction\_trim\_lines.txt

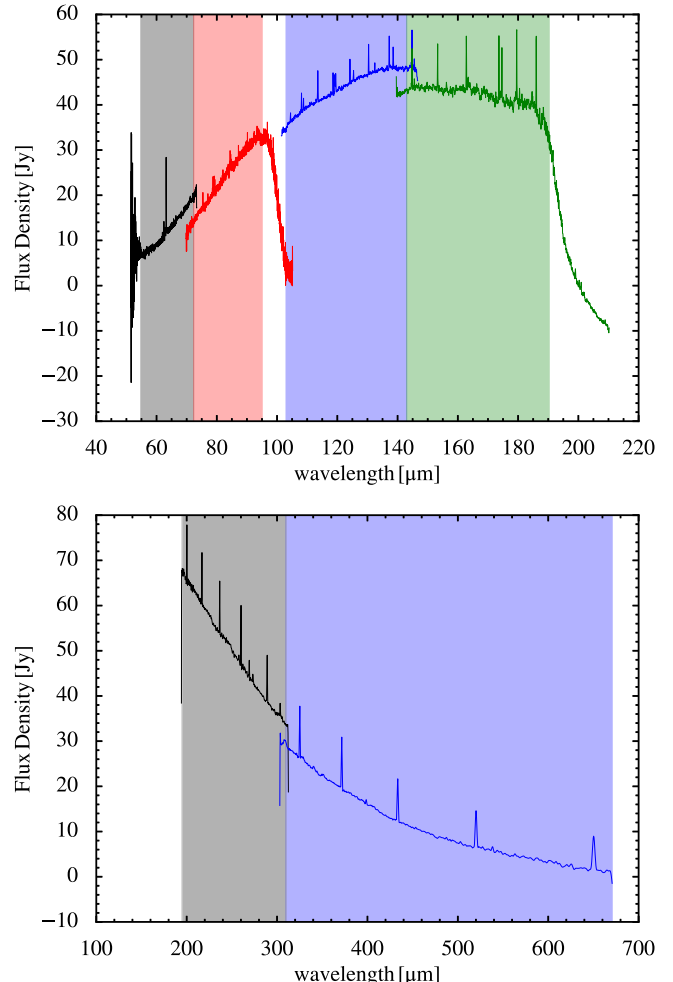


**Figure 14.** Original spectra of L1157, each module shown in a different color. The PACS spectra are shown at the top, while the SPIRE spectra are shown at the bottom. Note that the PACS spectra are shifted by  $-5\text{ Jy}$  between each module and the SPIRE spectra are shifted by  $5\text{ Jy}$  between two modules for better visualization of the overlap regions. The shaded area indicates the region where the spectrum with the same color is preserved after trimming.

```

Targetname_reduction_trim_continuum.txt
Targetname_reduction_trim_flat_spectrum.txt
Targetname_reduction_trim_residual_spectrum.txt
Targetname_pacs_pixel##_os##sf##_lines.txt
Targetname_pacs_pixel##_os##sf##_continuum.txt
Targetname_pacs_pixel##_os##sf##_flat_spectrum.txt
Targetname_pacs_pixel##_os##sf##_residual_spectrum.txt
(SPIRE)
Targetname_spire_corrected_lines.txt
Targetname_spire_corrected_continuum.txt
Targetname_spire_corrected_flat_spectrum.txt
Targetname_spire_corrected_residual_spectrum.txt

```

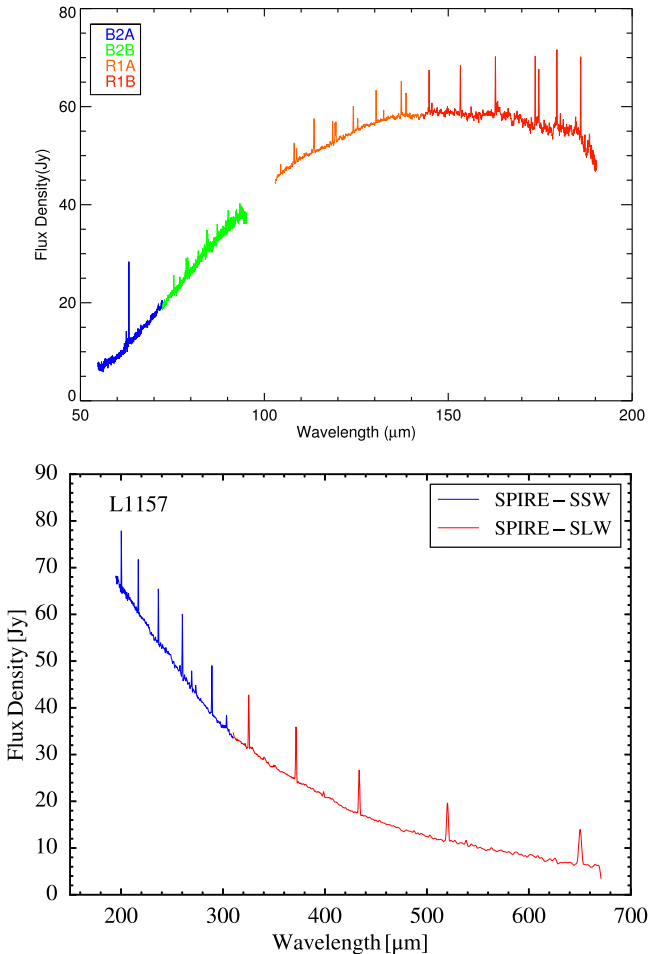


**Figure 15.** Top: an example 1D PACS spectrum of L1157, with the four modules highlighted by color. Bottom: an example 1D SPIRE spectrum of L1157, with the two modules highlighted by color.

Targetname\_pixelname\_lines.txt  
 Targetname\_pixelname\_continuum.txt  
 Targetname\_pixelname\_flat\_spectrum.  
 txt  
 Targetname\_pixelname\_redresidual\_spec-  
 trum.txt

The ASCII format line fitting results are presented in four output forms (lines, continuum, flat\_spectrum, and noise\_spectrum), as listed above. The first contains the full report of the line fitting results using the method described in Section 4, containing the fitted line parameters (Table 8) of each line in the full input list—including non-detections. Users can simply read this report and apply the fitting results. The second file contains the continuum spectrum of the source produced by subtracting the fitted lines from the original spectrum. The third file is the counterpart of the continuum file, a continuum-subtracted spectrum in which only the spectral lines and flat baseline remain (Figure 9). The fourth file contains the residual spectrum after the subtraction of fitted lines and smoothed continuum. The file names of PACS spectra are listed in the first block with the first four as the products of 1D spectra and last four as the products of 2D spectra, while file names of SPIRE spectra are listed in the second block with the same fashion.

(Fitting table including all sources)

CDF\_archive\_pacs\_1d\_lines.txt  
 CDF\_archive\_pacs\_cube\_lines.txt  
 CDF\_archive\_spire\_1d\_lines.txt  
 CDF\_archive\_spire\_cube\_lines.txt

The fitting results of 1D PACS, 1D SPIRE, 2D PACS, and 2D SPIRE of all sources are stored in separate ASCII files with similar tables to those described above and in Section 4 with an additional column with the object name, and a summary table that includes ALL fitting results (PACS, SPIRE, 1D, and 2D) is provided with a name of CDF\_archive\_lines.txt, in which the pixel column is labeled as ‘‘c’’ for 1D spectra.

(Individual line fitting plot in PACS)

spectrum\_line\_subtracted\_Targetna-  
 me\_reduction\_trim.eps  
 Targetname\_reduction\_trim\_linenam-  
 e.eps

Targetname\_reduction\_trim\_line1  
 +line2.eps (in ‘‘double\_gauss’’ folder)  
 (Individual line fitting plot in SPIRE)

Targetname\_spectrum\_line\_subrac-  
 ted\_spire\_corrected.eps  
 Targetname\_spire\_corrected\_linenam-  
 e.eps

Targetname\_spire\_corrected\_line1  
 +line2.eps (in ‘‘double\_gauss’’ folder)

The figures are all presented for typical spectra with various levels of data, as listed above. The first three of the six items are figures for PACS, while the last three of six are for SPIRE. The files with “spectrum\_line\_subtracted” provide overviews for line fitting results of each object and each instrument. It includes the original data (black), continuum (blue), and residual spectrum (green). The files with “linename” provide the visualization of the fitting result for each line (Figure 16 top). It includes original data (black), fitted line (blue), and residual/noise (green). The vertical lines represent the allowed region for line (dash line) and the region taken for the baseline fitting (dotted line). And the S/N and FWHM are printed within the figures. The fitting results of the double Gaussian, stored in ‘‘double\_gauss’’ folder, are plotted in figures with two lines in their file names (“line1+line2”) with an additional fitted line in orange (Figure 7). We also report the fitting results of the baseline in the subdirectory named “base” (Figure 16 bottom). The plot includes the original data (black), the fitted baseline (purple), residual (red), and the points taken in the baseline fitting (asterisks). There is another directory named “cannot\_fit” which includes the very rare case when the fitting failed to coverage.

#### (e) Quick look output for the fitting results

Filename:

Targetname\_reduction\_trim\_lines\_spe-  
 cies.txt  
 Targetname\_spire\_corrected\_species.  
 txt

This output provides the user a convenient quick look at the source spectral properties and evaluation of the fitting quality. These files contain the sorted line information of either the 1D spectrum or the spectrum of

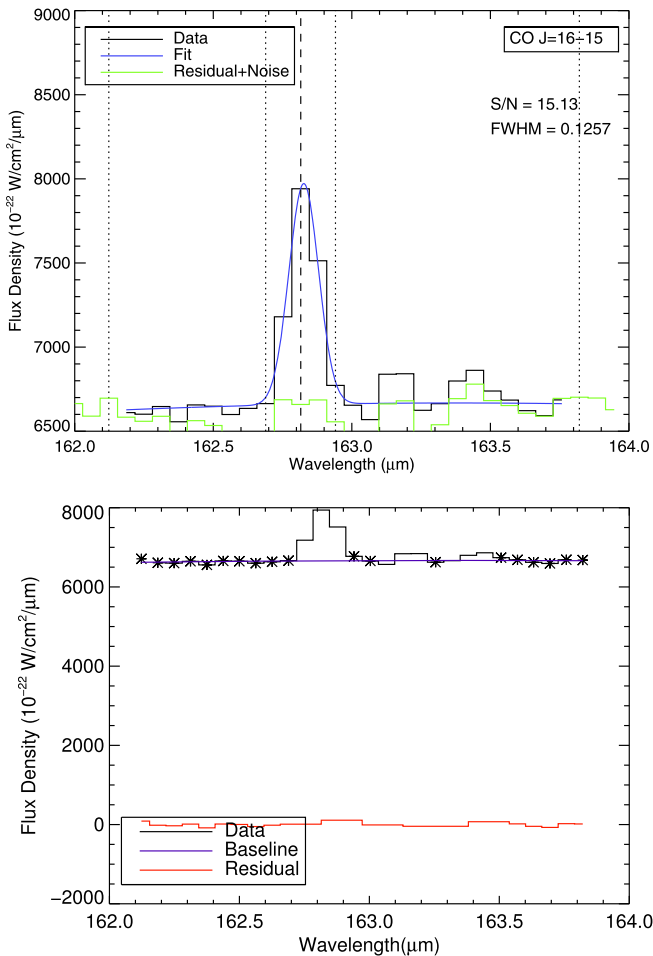


**Figure 16.** Top: an example of single line fitting result of CO  $J = 16 \rightarrow 15$  in L1157. Bottom: an example of the baseline fitting result at the region of CO  $J = 16 \rightarrow 15$  in L1157. The asterisks indicate the points used for the baseline fitting.

each spaxel for given molecular/atomic species. The line profiles of seven different species are separated including CO,  $^{13}\text{CO}$ ,  $\text{HCO}^+$ , OH, o-H<sub>2</sub>O, p-H<sub>2</sub>O, and atomic fine-structure transitions. The data for each molecule are stored in the corresponding files.

### 5.3. Comparison to Previously Published Results

The scientific implications of the reprocessed data archive will be reported in other papers. We note here the impact of the new archive on rotational temperatures and densities reported in Green et al. (2013a) and other works. We compared a sample of 18 sources with measured (PACS only) rotational temperatures and densities, divided into “warm” ( $\sim 300$  K) and “hot” ( $\sim 1000$  K) components as defined in previous papers, measured using the 2012-13 pipeline and again with the current pipeline. The rotational temperatures changed insignificantly: the average warm component temperature increased by 1.4% (ranging between  $-18\%$  and  $25\%$ ), while the average hot component temperature decreased by 1.5% (almost entirely due to one source, GSS 30-IRS1, decreasing by 7%). In contrast, the derived number densities were altered substantially. The average warm component increased in count by 17.6% (ranging from  $-27.5\%$  to  $62.5\%$ , with outlier GSS 30-IRS1 increasing by 198%). The hot component increased by 22%,

but this was entirely because of GSS 30-IRS1, which increased 107%; with that source omitted, the mean of the rest changed by less than 2%.

Thus the measured temperature values have changed only minimally, and the hot component was only slightly different except in cases where we properly captured the extended nature of the source in the new data products. In GSS 30-IRS1 in particular, we previously used the central spaxel only, and did not include extended emission; in this new analysis, we include the larger region. However, we do not attempt to disentangle GSS 30, as was done using earlier data products; Je et al. (2015) deconvolved GSS 30 into three separate IR sources. However, the increase in the warm component molecule number count is widespread in our sample, and is due to the calibration improvements in the long wavelengths of the PACS pipeline (100–190  $\mu\text{m}$ ).

In general, the adjustment in line flux does not impact previous results qualitatively. Green et al. (2013a) noted in Figure 23 that the low density solution in Neufeld (2012) was a good fit to the CO rotational diagram for B335; this conclusion is unchanged.

Lindberg et al. (2014) and Dionatos et al. (2013) considered complicated regions (RCrA and Serpens, respectively) and created prescriptions to deconvolve the sources therein. Our pipeline does not consider the deconvolution problem and we recommend using the earlier works. For example, Dionatos et al. (2013) find that the lines peak at the position of outflow shocks rather than the protostellar sources. This can be identified from the contour plots in our data set, and would require custom extraction techniques. We provide a well-calibrated spectrum for Serpens-SMM3 including the jitter correction; however the complex of shocks causes a different distribution of lines. Serpens-SMM4 was not successfully corrected for pointing jitter as noted in Table 1. Similarly, RCrA-IRS7B is calibrated via our pipeline, but RCrA-IRS7C is not successfully corrected. In each case, the earlier work uses line fluxes from spaxels associated with outflow shocks rather than the continuum (protostellar) sources. Both find that the rotational temperatures of the spaxels dominated by shocks are similar to those toward the protostar, but the number of molecules is different. In each case, we expect that using our new data set would provide reduced absolute calibration and line flux uncertainty, but the deconvolution would still be required as post-processing.

The case of L1448-MM (Lee et al. 2013) is similar, but the central source dominates the continuum and line fluxes. Thus the deconvolution is required to separate L1448-C, N, and S, but the overall results for the dominant submillimeter source L1448-MM are not significantly changed.

Finally, the FOOSH data set included both an earlier SPIRE and PACS reduction, and 4 of those objects appear in this data set. The warm (PACS) component was only detected in V1057 Cyg and the temperature has increased by a factor consistent with the DIGIT PACS sources, 17%, with a similar decrease in number, consistent with the spread in changes seen in the DIGIT sample. However, some of the SPIRE data are significantly changed. FU Ori still includes no significant CO detections in the SPIRE bands. V1057 Cyg exhibited a well-characterized cool component which was essentially unchanged ( $\sim 3\%$ ). V1515 Cyg and V1331 Cyg had only 3 detections in the earlier work; V1331 Cyg now has 6 CO lines detected, and this has altered the rotational properties

considerably. The cool CO rotational temperatures increased in both sources, from  $\sim$ 20–30 K to 75–100 K, and the number of molecules dropped by a factor of 2. We conclude that the improvement in absolute flux calibration can dramatically change the number of molecules detected in the SPIRE bands, and the correction for extended sources can alter the temperature.

## 6. CONCLUSIONS

We have provided a data set of *Herschel*-PACS and SPIRE spectroscopy to generate a broadly accessible archive with easily downloaded data products (grids of maps, continuum, lines, and full SEDs) of publishable quality. This data set will complement and enhance the HSA, to serve the community with a Legacy Archive for young stellar objects. Expected legacy investigations will reveal fundamental constraints on accretion processes, environments of protostars, and the conditions in emerging protoplanetary disks.

J.D.G. would like to acknowledge numerous helpful discussions with the PACS and SPIRE ICC teams, via webinars, helpdesk queries, and contacts. Support for this work, part of the *Herschel* Open Time Key Project Program, was provided by NASA through awards issued by the Jet Propulsion Laboratory, California Institute of Technology. The research of J.-E.L. was supported by the 2013 Sabbatical Leave Program of Kyung Hee University (KHU-20131724) and also supported by Basic Science Research Program through the National Research Foundation of Korea (NRF) funded by the Ministry of Science, ICT and future Planning (2015R1A2A2A01004769). J.D.G. and Y.-L.Y. acknowledge support from NASA *Herschel* Science Center Cycle 2 grants. R.L. acknowledges support from the Karl G. Henize Endowed Scholarship, the John W. Cox Endowment for the Advanced Studies in Astronomy, and the College of Natural Sciences Summer Undergraduate Research Fellowship at the University of Texas at Austin. AK acknowledges support from the Foundation for Polish Science (FNP) and the Polish National Science Center grant 2013/11/N/ST9/00400.

## APPENDIX

### SOURCELIST AND DATA PRODUCT STATUS

The comprehensive source list, OBSID number, R.A., decl., and reduction type are listed in Table 1.

## REFERENCES

- Authier, N., Bagland, N., & Lefloch, A. 1993, JMoSp, 160, 590
- Balog, Z., Müller, T., Nielbock, M., et al. 2014, ExA, 37, 129
- Bendo, G. J., Griffin, M. J., Bock, J. J., et al. 2013, MNRAS, 433, 3062
- Ceccarelli, C., Caux, E., Loinard, L., et al. 1999, A&A, 342, L21
- Cieza, L. A., Olofsson, J., Harvey, P. M., et al. 2013, ApJ, 762, 100
- Dionatos, O., Jørgensen, J. K., Green, J. D., et al. 2013, A&A, 558, A88
- Dunham, M. M., Evans, N. J., Terebey, S., Dullemond, C. P., & Young, C. H. 2010, ApJ, 710, 470
- Dunham, M. M., Stutz, A. M., Allen, L. E., et al. 2014, in Prostars and Planets VI, ed. H. Beuther et al. (Tucson, AZ: Arizona Press), 195
- Evans, N. J., Dunham, M. M., Jørgensen, J. K., et al. 2009, ApJS, 181, 321
- Flower, D. R., & Pineau Des Forets, G. 2010, MNRAS, 406, 1745
- Giannini, T., Lorenzetti, D., Tommasi, E., et al. 1999, A&A, 346, 617
- Giannini, T., Nisini, B., & Lorenzetti, D. 2001, ApJ, 555, 40
- Goorvitch, D. 1994, ApJS, 95, 535
- Green, J. D., Evans, N. J., II, Jørgensen, J. K., et al. 2013a, ApJ, 770, 123
- Green, J. D., Evans, N. J., II, Kóspál, Á., et al. 2013b, ApJ, 772, 117
- Griffin, M. J., Abergel, A., Abreu, A., et al. 2010, A&A, 518, L3
- Higdon, S. J. U., Devost, D., Higdon, J. L., et al. 2004, PASP, 116, 975
- Je, H., Lee, J.-E., Lee, S., Green, J. D., & Evans, N. J., II 2015, ApJS, 217, 6
- Karska, A., Herczeg, G. J., van Dishoeck, E. F., et al. 2013, A&A, 552, A141
- Kaufman, M. J., & Neufeld, D. A. 1996, ApJ, 456, 611
- Kim, H. J., Evans, N. J., II, Dunham, M. M., Lee, J.-E., & Pontoppidan, K. M. 2012, ApJ, 758, 38
- Kristensen, L. E., van Dishoeck, E. F., Bergin, E. A., et al. 2012, A&A, 542, A8
- Lahuis, F., Kessler-Silacci, J. E., Knez, C., et al. 2006, c2d Spectroscopy Explanatory Supplement (Pasadena, CA: Spitzer Science Center)
- Lee, J., Lee, J.-E., Lee, S., et al. 2013, ApJS, 209, 4
- Lindberg, J. E., Jørgensen, J. K., Green, J. D., et al. 2014, A&A, 565, A29
- Lorenzetti, D., Giannini, T., Nisini, B., et al. 2000, A&A, 357, 1035
- Lorenzetti, D., Tommasi, E., Giannini, T., et al. 1999, A&A, 346, 604
- Markwardt, C. B. 2009, in ASP Conf. Ser. 411, Astronomical Data Analysis Software and Systems XVIII, ed. D. A. Bohlender, D. Durand, & P. Dowler (San Francisco, CA: ASP), 251
- Müller, H., Schlöder, F., Stutzki, J., & Winnewisser, G. 2005, JMoSt, 742, 215
- Müller, T., Balog, Z., Nielbock, M., et al. 2014, ExA, 37, 253
- Neufeld, D. A. 2012, ApJ, 749, 125
- Nisini, B., Benedettini, M., Codella, C., et al. 2010, A&A, 518, L120
- Nisini, B., Giannini, T., & Lorenzetti, D. 2002, ApJ, 574, 246
- Offner, S. S. R., & McKee, C. F. 2011, ApJ, 736, 53
- Palla, F., & Stahler, S. W. 1993, ApJ, 418, 414
- Poglitsch, A., Waelkens, C., Geis, N., et al. 2010, A&A, 518, L2
- Rebull, L. M., Padgett, D. L., McCabe, C.-E., et al. 2010, ApJS, 186, 259
- Schöier, F. L., van der Tak, F. F. S., van Dishoeck, E. F., & Black, J. H. 2005, A&A, 432, 369
- Shirley, Y. L., Evans, N. J., II, Rawlings, J. M. C., & Gregeren, E. M. 2000, ApJS, 131, 249
- van Dishoeck, E. F., Kristensen, L. E., Benz, A. O., et al. 2011, PASP, 123, 138
- Wampfler, S. F., Bruderer, S., Karska, A., et al. 2013, A&A, 552, A56
- Ward-Thompson, D., André, P., Crutcher, R., et al. 2007, in Protostars and Planets V, ed. B. Reipurth, D. Jewitt, & K. Keil (Tucson, AZ: Univ. Arizona Press), 33
- Wu, J., Dunham, M. M., Evans, N. J., II, Bourke, T. L., & Young, C. H. 2007, AJ, 133, 1560
- Wu, R., Polehampton, E. T., Etxaluze, M., et al. 2013, A&A, 556, A116
- Yang, B., Stancil, P. C., Balakrishnan, N., & Forrey, R. C. 2010, ApJ, 718, 1062
- Young, C. H., Bourke, T. L., Young, K. E., et al. 2006, AJ, 132, 1998